

28 of the novel SS-JDL method was tested on aerial digital photography of three complex and
29 heterogeneous landscapes, two in Southern England (Bournemouth and Southampton) and one
30 in North West England (Manchester). Benchmark comparisons were provided in the form of a
31 range of LU and LC methods, including the state-of-the-art joint deep learning (JDL) method.
32 The experimental results demonstrated that the SS-JDL consistently outperformed all of the
33 state-of-the-art baselines in terms of both LU and LC classification accuracies, as well as
34 computational efficiency. The proposed SS-JDL method, therefore, represents a fast and
35 effective implementation of the state-of-the-art JDL method. By creating a single, unifying
36 joint distribution framework for classifying higher order feature representations, including LU,
37 the SS-JDL method has the potential to transform the classification paradigm in remote
38 sensing, and in machine learning more generally.

39 **Keywords:** multi-scale deep learning; optimal scale selection; convolutional neural network; joint
40 classification; hierarchical representations

41 **1 Introduction**

42 Land use and land cover (LULC) information is essential for diverse applications in geospatial
43 domain, such as urban and regional planning, environmental monitoring and management (Liu
44 *et al.*, 2017, Zhang *et al.*, 2019). LULC information can also provide insights to tackle a
45 multitude of socioeconomic and environmental challenges, including food insecurity, poverty,
46 climate change and disaster risk (Stürck *et al.*, 2015). Recent advances in sensor technologies
47 have led to a constellation of satellite and airborne platforms, from which a large amount of very
48 fine spatial resolution (VFSR) remotely sensed imagery is available commercially. While great
49 opportunities are offered by VFSR imagery to capture fine-grained LULC detail, information
50 extraction and retrieval is still immature and inefficient, primarily undertaken by means of
51 traditional field survey and manual interpretation (Hu and Wang, 2013). Such routine tasks are
52 labour-intensive and time-consuming. At the same time, our environment is constantly changing
53 requiring frequent updates of LULC information to support scientific decision-making. It is,

54 therefore, of paramount importance to develop highly efficient and effective techniques to derive
55 LULC information in an automatic and intelligent fashion.

56 Over the past twenty years, significant efforts have been made towards the automation of LULC
57 classification methods using VFSR images. Traditional techniques can be categorised into pixel-
58 based and object-based approaches. Pixel-based methods focus on classifying individual pixels
59 based on spectral reflectance, which often result in speckle noise effects with limited
60 classification accuracy, given the spectral and spatial complexity presented in VFSR remotely
61 sensed imagery. Textures (Herold *et al.*, 2003) and contextual information (Wu *et al.*, 2009) can
62 be integrated to characterise spatial patterns using moving kernels or windows. These approaches,
63 however, are built on arbitrarily structured images (e.g. squares), whereas real world objects are
64 often irregularly shaped and structured in specific patterns (Herold *et al.*, 2003). Object-based
65 methods are now adopted widely for LULC image classification based on segmented objects
66 (group of pixels), thereby allowing the extraction of discriminative features (e.g., spectral,
67 texture, shape) within the objects and contextual information between adjacent regions. However,
68 those object-based approaches are often challenged by selecting appropriate segmentation scales
69 to achieve meaningful objects (e.g., particular land cover categories), with under- and over-
70 segmentation occurring within the single image (Ming *et al.*, 2015). Besides, the extracted
71 features that characterise the objects are essentially hand-coded via feature engineering, which
72 is subject to individual user experience and expertise, making it difficult to achieve comparable
73 results when transferring the classifier to other datasets. Additionally, the spatial configurations
74 of land use objects can be extremely difficult to hand-code into explicit features, thus, limiting
75 representation and discrimination through traditional methods. Moreover, traditional methods
76 lack a clear definition of the classification hierarchy (i.e. the level of representations of the
77 landscape) and LULC classes are often used interchangeably in remotely sensed image
78 classification. Ontologically, however, land cover (LC) and land use (LU) are manifested at

79 different levels of representation: LC represents low-level states whereas LU characterises high-
80 level functions of the landscape.

81 Recently, deep learning-based methods have attracted enormous interest in the field of pattern
82 recognition and computer vision, owing to their capability to learn the most representative and
83 discriminative features hierarchically in an end-to-end fashion (Arel *et al.*, 2010). Deep
84 convolutional neural network (CNN), as a popular deep learning method, has achieved
85 significant breakthroughs in image processing and analysis (Krizhevsky *et al.*, 2012), with
86 impressive results beyond the state-of-the-art in a variety of disciplines, not only in classical
87 computer vision fields such as visual recognition, target detection and robotics, but also in many
88 other practical applications (Hu *et al.*, 2015; Nogueira *et al.*, 2017). In the remotely sensed
89 domain, the CNN has shown huge potential in diverse tasks through high-level feature
90 representations, such as road extraction (Cheng *et al.*, 2017), vehicle detection (Dong *et al.*,
91 2015), scene classification (Liu *et al.*, 2018), semantic segmentation (Wang *et al.*, 2017), and
92 LULC image classification (Zhang *et al.*, 2018a; 2018b).

93 Within a CNN network, a patch-based architecture is used to learn and extract higher-level
94 features in image patches autonomously through a hierarchy of filters. As a consequence, the
95 choice of image patch size, as a key CNN parameter, has a significant influence on the scale of
96 representations that are manifested over the landscape and, consequently, the accuracy of
97 remotely sensed image classification. These scales are also dependent on the definition of the
98 LULC classification hierarchy, which is unclear so far. Therefore, the determination of the CNN
99 scale for a specific LULC classification task is still an open question in the remote sensing
100 community, and a common approach is to consider scale variations, that is, not constrain to a
101 single scale representation (Pan and Zhao, 2018). Previous research has attempted to incorporate
102 multiple scales into the CNN network to improve spatial feature representations across different
103 scales (e.g., Lv *et al.*, 2018; Yang *et al.*, 2018; Zhang *et al.*, 2018b). For example, a set of CNNs

104 with different patch sizes and scales were integrated by Deng *et al.* (2018) and Liu *et al.* (2018)
105 to enhance feature representations across multiple scales, thereby achieving increased accuracy
106 of scene classification. Yang *et al.* (2018) utilised multi-scale CNNs to differentiate complex
107 scenes (e.g., airport, residential, commercial) in remotely sensed imagery, and demonstrated
108 increased accuracy compared with single-scale CNN networks. Deep features at a range of scales
109 have also been embedded into the CNN to identify vehicles (e.g., ships, cars) within remotely
110 sensed scenes, leading to increased accuracy of target detection (Li *et al.*, 2018). In remotely
111 sensed image classification, Lv *et al.* (2018) combined region-based CNNs at multiple scales to
112 differentiate land cover objects with high accuracy and efficiency. In addition, object-based
113 CNNs comprising of two distinctive scales were developed to solve the complex land *use*
114 classification task (Zhang *et al.*, 2018b). Finally, deep features at multiple scales were extracted
115 through CNN networks, and used to boost land cover classification accuracy for hyperspectral
116 images (He *et al.*, 2019). A challenge for these multi-scale CNN techniques, however, is to
117 determine the optimal scales (patch sizes) from a large sampling space that is extremely difficult
118 to explore exhaustively across the full range of scales.

119 In summary, current LULC classification approaches (both traditional and deep learning
120 methods) suffer from two major issues: (1) definition of the classification hierarchy; and (2)
121 definition of the optimal scale to represent the landscape. In terms of the classification hierarchy,
122 land use (LU) and land cover (LC) are often defined interchangeably, without differentiating
123 their intrinsic differences in semantic meaning. LC represents the physical characteristics of the
124 Earth's surface, whereas LU is defined as a higher-order function within a particular space
125 through a mosaic of different LC categories. The spatially nested and hierarchical relationships
126 between LU and LC are given little consideration in LULC image classification, except for the
127 recently proposed joint deep learning (JDL) method (Zhang *et al.*, 2019). As for the choice of
128 scale, it is challenging to determine an optimal scale that can represent the entire scene of a

129 complex and heterogeneous landscape, and multi-scale feature representations are often
130 incorporated to capture large or small land features over different scales. These multiple scales
131 are searched exhaustively through trial and error and tested through extensive experiments with
132 different combinations of candidate scales (Kim *et al.*, 2011; Ming *et al.*, 2015). For deep
133 learning methods (e.g., CNN), such scale parameterisation processes are extremely time-
134 consuming with a large amount of CNN model training. The process can be labour-intensive
135 with repetitive experiments, especially for joint LU and LC classification such as through the
136 JDL method. Furthermore, the selected multiple scales are considered independently as
137 individual evidence to support integrated decisions, which do not capture the mutual connections
138 among the different scales. As such, these scale selection processes are far from operational for
139 deep learning in remotely sensed image classification.

140 The objective of this research was to develop an automatic approach that is applicable in
141 engineering practices to model the nested relationships between LU and LC, with the ability to
142 address scale issues effectively and efficiently in remotely sensed image classification. A novel
143 scale sequence joint deep learning (SS-JDL) method for LU and LC classification is proposed,
144 in which, scales (input patch sizes) of the CNN networks are autonomously derived as a sequence
145 of representations. The scale sequence is designed to mimic the human cognition of image
146 pattern recognition through continuously increasing scales, with information transmission
147 between neighbouring scales from small-scale features to large-scale visual representations. The
148 SS-JDL has the key advantage that it is simple and parsimonious in the way that it constructs the
149 sequence of scales and determines an efficient solution, such that the cumbersome and time-
150 consuming process of optimal scale selection is avoided. The rest of the paper is organized as
151 follows: the proposed method is detailed in section 2; followed by experiments and results
152 analysis in section 3; discussions and conclusions are made in section 4 and 5, respectively.

153 **2 Methods**

154 2.1 Multilayer perceptron (MLP)

155 A multilayer perceptron (MLP) is a feed forward neural network that transforms the input data
156 (e.g., image pixels) into the output representations (e.g., LC labels) (Atkinson and Tatnall, 1997).
157 Typically, a MLP is composed of input, hidden, and output layers with computational nodes
158 fully connected by weights and biases (Del Frate *et al.*, 2007). These weights and biases are
159 learned through backpropagation using a specific loss function (e.g., cross-entropy), to minimise
160 the distinction between model predictions and the desired results.

161 2.2 Convolutional Neural Networks (CNN)

162 A convolutional neural network (CNN) takes an image patch (a group of pixels) as its input to
163 predict high level feature representations (e.g., LU categories). The CNN network is basically
164 cascaded by multiple convolutional, max-pooling, and batch normalisation layers to characterise
165 the functional semantics at abstract and deep levels. Specifically, the convolutional layers
166 involve a kernel function to convolve across input feature maps to recognise spatial features,
167 followed by an activation function, such as Rectified Linear Unit, to strengthen and enhance the
168 non-linearity. The max-pooling layers sub-sample the feature maps to enhance the generalisation
169 capability with a reduced number of parameters (Romero *et al.*, 2016). The batch normalisation
170 layers are used to accelerate the training process of the deep network by standardising the training
171 sample batches (Li *et al.*, 2018). The parameters within the CNN network (e.g., kernel weights
172 and biases) are learnt by a stochastic gradient descent in a feed-forward fashion (LeCun *et al.*,
173 2015). Finally, a fully connected layer is utilised together with a softmax classification to predict
174 the final output.

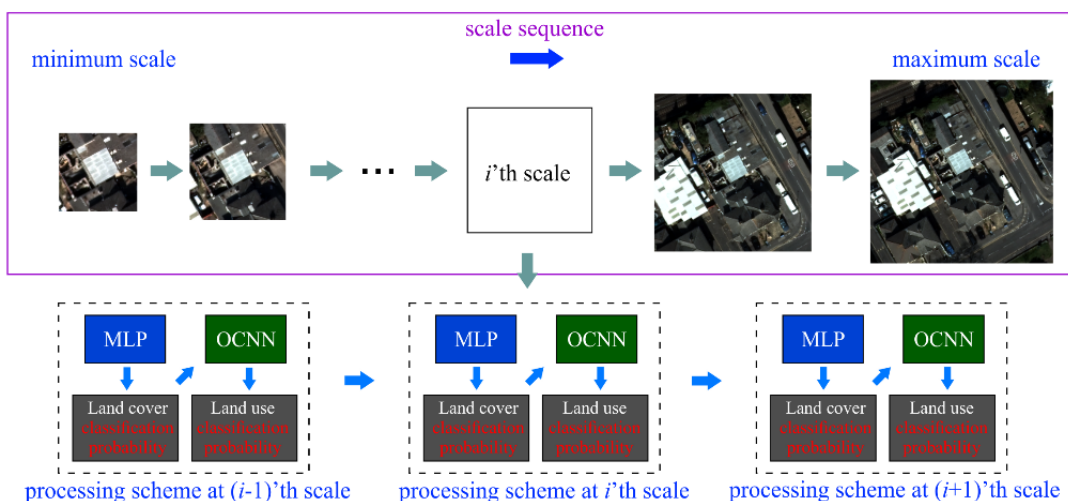
175 2.3 Object-based Convolutional Neural Network (OCNN)

176 Object-based CNNs (OCNN) were designed on the basis of CNN models to classify segmented
177 objects into specific LU classes (Zhang *et al.*, 2018c). Different from the standard pixel-wise

178 CNN that predicts image patches densely overlap at the pixel level, the OCNN places an image
 179 patch at the centroid of an object for prediction, which significantly enhances the computational
 180 efficiency while reducing the uncertainties caused by the convolutional process (e.g., geometric
 181 distortion). The image patch size is empirically tuned as sufficiently large to capture patterns of
 182 objects and their contexts. In Zhang *et al.* (2018c), the OCNN was trained to learn LU semantics
 183 through deep networks, and the boundaries of each object were maintained through image
 184 segmentation. The prediction of LU for each object was then assigned to the constituent pixels
 185 to formulate the final land use thematic map.

186 2.4 Scale sequence joint deep learning (SS-JDL)

187 The proposed scale sequence joint deep learning (SS-JDL) method has two major aspects: the
 188 creation and use of a scale sequence and joint learning between the LU and LC predictions at
 189 each scale in the scale hierarchy. The scale sequence is composed of a set of observational scales
 190 (image patch sizes) that transfers the information from a small scale to larger scales sequentially,
 191 in which fine details produced by convolution over a small window are integrated into a broader
 192 context through convolution over increasingly larger windows. Within each scale, the LU and
 193 LC are represented at different classification hierarchies and jointly classified through iteration.
 194 The general procedure of the proposed SS-JDL method is illustrated by Figure 1, where the LU
 195 and LC classifications are jointly derived across the scale sequence.



196

197 Figure 1. The general workflow of scale sequence joint deep learning (SS-JDL) for land cover and land
198 use classification

199 In the SS-JDL method, a scale sequence (denoted as the set \mathbf{S}) is needed to characterise the LU
200 and LC across different scales. The \mathbf{S} requires the parameterisation of the minimum scale (θ_{\min}),
201 the maximum scale (θ_{\max}), and the total number of elements within \mathbf{S} (n), in which the scale is
202 derived by Eq. 1 as:

$$203 \quad \mathbf{S} = \text{Linspace}(\theta_{\min}, \theta_{\max}, n) \quad (1)$$

204 Where, *Linspace* refers to the function of linear interpolation. By using Eq. 1, a scale sequence
205 $\mathbf{S} = (s_1, s_2, \dots, s_i, \dots, s_n)$ is obtained, in which s_i ($i \in [1, n]$) corresponds to the i -th scale value.
206 Both θ_{\min} and θ_{\max} are computed based on the sizes of objects segmented from the imagery. The
207 θ_{\min} is equal to or smaller than the minor axis of the smallest object, whereas the θ_{\max} is larger
208 than the major axis of the largest object.

209 At each scale, the LU and LC classifications are derived from a pixel-based MLP classifier and
210 a patch-based OCNN classifier, respectively (Zhang *et al.*, 2019). The LU classification
211 probabilities are conditional on the LC classification probabilities, and the results of i -th iteration
212 are influenced by the previous iteration. Such a hierarchical classification framework is
213 formulated as a Markov process as:

$$214 \quad P(\text{LU}(\theta)^i, \text{LC}^i) = P(\text{LU}(\theta)^i, \text{LC}^i \mid \text{LU}(\theta)^{i-1}, \text{LC}^{i-1}) \quad (2)$$

215 Where i denotes the number of iterations within the Markov process. The θ parameter provides
216 the CNN input window size as the scale of the current iteration. The $\text{LU}(\theta)^i$ in Eq. 2 refers to the
217 LU classification probabilities at the i -th iteration. The LC^i corresponds to the land cover
218 classification probabilities at the i -th iteration.

219 Given a scene of remotely sensed imagery $M(x, y)$ with x and y representing the spatial
 220 coordinates, the training samples of LU and LC are described as $\mathbf{T}_{LC} = (t_{LC1}, t_{LC2}, \dots, t_{LCi}, \dots,$
 221 $t_{LCu})$ and $\mathbf{T}_{LU} = (t_{LU1}, t_{LU2}, \dots, t_{LUi}, \dots, t_{LUv})$, where u and v denote the total numbers of LU and
 222 LC training samples, respectively, and t_{LCi} and t_{LUi} refer to the i -th samples of LU and LC
 223 respectively. $t_{LCi} = \{x_i, y_i, \mathcal{L}_{LC}\}$ refers to the LC class label (\mathcal{L}_{LC}) of the i -th sample and its spatial
 224 location (x_i, y_i) on imagery M , whereas $t_{LUi} = \{x_i, y_i, \mathcal{L}_{LU}\}$ denotes the LU class label (\mathcal{L}_{LU}) and
 225 its position (x_i, y_i) in image M . The \mathbf{T}_{LC} and \mathbf{T}_{LU} were used to train the MLP and OCNN models
 226 to predict the LU and LC classification probabilities, respectively (Figure 1).

227 Based on Eq. 2, for the image M , the classification results of LU at previous iteration $LU(\theta)^{i-1}$
 228 (NULL for the first iteration), LC samples \mathbf{T}_{LC} , LU samples \mathbf{T}_{LU} , and the scale value of the
 229 current iteration θ serve as the input data and parameters. The probabilistic outputs of the LC
 230 ($M_{LCpro}(i)$) and LU ($M_{LUpro}(i)$) classifications are achieved through the iterative process. Detailed
 231 methods for achieving LU and LC classification probabilities and their output maps are
 232 demonstrated as follows:

233 (i) LC classification probabilities

234 LU classification probabilities at previous iteration $LU(\theta)^{i-1}$ and the original image M are
 235 integrated as conditional probabilities for land cover classification (M_{LC}^i) as:

$$236 \quad M_{LC}^i = \text{Concate}(M, LU(\theta)^{i-1}) \quad (3)$$

237 Where, *Concate* is a function to concatenate the image M with the LU classification probabilities
 238 at the previous iteration ($i-1$). Note, Eq. 3 corresponds to the case of $i > 1$. If $i=1$, M_{LC}^i is equivalent
 239 to the original image M as the LU probabilities are empty (NULL) initially.

240 Based on Eq. 3, the MLP model is trained through the LC training samples (\mathbf{T}_{LC}) as follows:

$$241 \quad mlpmodel^i = \text{MLP.Train}(M_{LC}^i, \mathbf{T}_{LC}) \quad (4)$$

242 The trained MLP model ($mlpmodel^i$) at the i -th iteration is used to predict the LC classification
 243 probabilities (M_{LCpro}^i) as:

$$244 \quad M_{LCpro}^i = mlpmodel^i.Predict(M_{LC}^i) \quad (5)$$

245 Here, the extent of M_{LCpro}^i is equal to the size of image M , and the dimensions of M_{LCpro}^i are the
 246 same as the number of LC classes, with each dimension corresponding to the probabilities of a
 247 specific LC class predicted by the MLP classifier.

248 (ii) LU classification probabilities

249 LC classification probabilities derived from the MLP (M_{LCpro}^i) are taken as the input image (M_{LU}^i)
 250 for LU classification. The CNN model is trained by using \mathbf{T}_{LU} as:

$$251 \quad cnnmodel^i = CNN.Train(M_{LU}^i, \mathbf{T}_{LU}, \theta^i) \quad (6)$$

252 The $cnnmodel^i$ model is further used to classify the image M_{LU}^i to link the LC probabilities with
 253 the LU classifications, and the LU classification probabilities (M_{LUpro}^i) are obtained as follows:

$$254 \quad M_{LUpro}^i = cnnmodel^i.Predict(M_{LU}^i) \quad (7)$$

255 In Eq. 7, the object-based CNN is adopted for LU classification (Zhang *et al.*, 2018c), by which
 256 the prediction of the $cnnmodel^i$ is assigned to the constituent pixels of the corresponding object.
 257 M_{LUpro}^i has the same image size as M , and the dimension is equal to the number of LU classes,
 258 with each dimension corresponding to the softmax probabilities acquired at the last layer of the
 259 CNN model.

260 Both land cover (M_{LCpro}^i) and land use (M_{LUpro}^i) probabilities are achieved in each iteration. The
 261 output at the final iteration (n) comprises M_{LCpro}^n and M_{LUpro}^n , where the LU and LC thematic
 262 maps are acquired as:

$$263 \quad M_{LCresult} = \arg \max(M_{LCpro}^n) \quad (8)$$

264
$$M_{LUresult} = \arg \max(M_{LUpro}^n) \quad (9)$$

265 In Eqs. 8 and 9, the probabilistic land cover (M_{LCpro}^n) and land use (M_{LUpro}^n) are converted into
266 the corresponding LC ($M_{LCresult}$) and LU ($M_{LUresult}$) classes by outputting the maximum
267 probabilities, respectively.

268 Essentially, the SS-JDL method inherits all the benefits of the JDL method (Zhang *et al.*, 2019)
269 which are:

- 270 1. Joint classification of LU and LC in an automatic manner.
271 2. Increased classification accuracies for LU and LC through joint reinforcement.
272 3. Faithful representation of the hierarchical relationships between LU and LC
273 characterisations.
274 4. Increased model robustness and generalisation capability with small sample size
275 requirement for the CNN.

276 Combining scale sequencing with the JDL method brings three additional benefits:

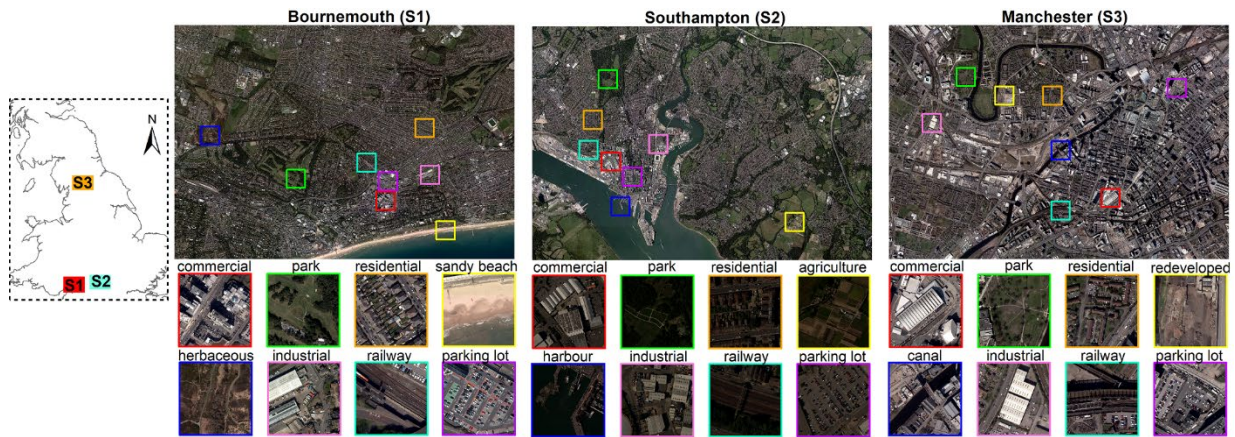
- 277 1. Incorporation of a sequence of scales (patch sizes) within a single unified JDL
278 framework.
279 2. Increased computational efficiency with rapid convergence to the optimal solution
280 through simple and parsimonious scale sequence.
281 3. Autonomous implementation without the need to choose a specific or optimal scale of
282 analysis.

283 **3 Experiment and Results**

284 3.1 Study area and data materials

285 Three study areas, including Bournemouth (S1), Southampton (S2) and Manchester (S3), and
286 their surrounding terrestrial regions (Figure 2) were chosen in this research. Both S1 and S2 lie

287 on the southern coast of England, whereas S3 is located inland in the north west of England. S1
 288 represents a mixture of anthropogenic and semi-natural environments (e.g., Queen’s Park Golf
 289 Course, Heath). S2 is a major port influenced by human activities in both urban and rural settings
 290 (e.g., large-scale industry, agriculture), whereas S3 is a major inland city and metropolitan
 291 borough with a high-density of urban and suburban areas notable for its commercial and social
 292 impact. They are, therefore, highly distinctive and heterogeneous in both LU and LC
 293 configurations and are, thereby, able to be used to test the generalisation ability of the proposed
 294 method.



295
 296 Figure 2. Three study areas: Bournemouth (S1), Southampton (S2) and Manchester (S3) in England,
 297 with typical land use categories highlighted for each study site.

298 Aerial photos of S1 (23,070×18,526 pixels), S2 (23,250×17,500 pixels) and S3 (17,590×14,360
 299 pixels) composed of four spectral bands (R, G, B and NIR) with 50-cm spatial resolution, were
 300 captured by Vexcel UltraCam Xp digital aerial cameras on 20 April 2016, 22 July 2012, and 20
 301 April 2016, respectively. Ten, nine and nine LC categories were recognised in S1, S2, and S3,
 302 respectively (Table 1). Eight LC classes appear consistently at three study sites: *Concrete Roof*,
 303 *Clay Roof*, *Metal Roof*, *Asphalt*, *Bare Soil*, *Rail*, *Grassland*, and *Woodland*. The remaining two
 304 LC classes in S1 were *Heath* and *Sand*, the one in S2 was *Crops*, and the one in S3 was *Water*.
 305 Those LCs characterise the physical characteristics of the ground surface, whereas the LUs
 306 represent functional use induced by human beings. Eleven LU types, including *Commercial*,

307 *Industrial, Residential, Institutional, Highway, Railway, Parking Lot, Park and Recreational*
308 *Area, Redeveloped Area, Herbaceous Vegetation, and Sandy Beach*, were identified in S1. As
309 for S2, 10 major types of LUs were involved, namely, *Commercial, Industrial, Medium-density*
310 *Residential, High-density Residential, Railway, Highway, Parking Lot, Redeveloped Area, Park*
311 *and Recreational Area*, and *Agricultural Area*. In terms of S3, nine main LU categories were
312 found, including: *Commercial, Industrial, Residential, Railway, Highway, Parking Lot,*
313 *Redeveloped Area, Park and Recreational Area, and Canal*. These LU and LC classes were
314 defined based on the European Environment Agency Urban Atlas 2012 and the Land Cover Map
315 2015 produced by NERC Centre for Ecology & Hydrology, together with the UK national land
316 use system developed by Ministry of Housing, Communities and Local Government. Detailed
317 LU classes and their sub-classes as well as major LC components were listed in Table 1.

318 Table 1. The land use (LU) classes with their sub-class descriptions, and the associated major land cover
319 (LC) components across the three study sites (S1, S2 and S3).

| LU | Study site | Sub-class descriptions | Major LC |
|------------------------------|------------|--|--------------------------------|
| (High-density) residential | S1, S2, S3 | Residential houses, terraces, green space | Buildings, Grassland, Woodland |
| (Medium-density) residential | S2 | Residential flats, green space, parking lots | Buildings, Grassland, Asphalt |
| Commercial | S1, S2, S3 | Shopping centre, retail parks, commercial services | Buildings, Asphalt |
| Industrial | S1, S2, S3 | Marine transportation, car factories, gas industry | Buildings, Asphalt |
| Highway | S1, S2, S3 | Asphalt road, lane, cars | Asphalt |
| Railway | S1, S2, S3 | Rail tracks, gravel, sometimes covered by trains | Rail, Bare soil, Woodland |
| Parking lot | S1, S2, S3 | Asphalt road, parking line, cars | Asphalt |
| Park and recreational area | S1, S2, S3 | Green space and vegetation, bare soil, lake | Grassland, Woodland |
| Redeveloped area | S1, S2, S3 | Bare soil, scattered vegetation, reconstructions | Bare soil, Grassland |
| Sandy beach | S1 | Costal line, sand, seaside beaches | Asphalt, Bare soil |
| Herbaceous Vegetation | S1 | Grasses and Forbs, shrubs | Grassland, Woodland |
| Agricultural area | S2 | Pastures, arable land, and permanent crops | Crops, Grassland |
| Canal | S3 | Water drainage channels, canal water | Water, Asphalt |

320

321 Reference polygons for LU and LC are collected by field surveyors and manually digitised by
322 photogrammetrists at Ordnance Survey (Britain’s National Mapping Agency). These reference
323 polygons (covering the majority of study sites) were split randomly into 60% for training and
324 40% for validation. Sample points were chosen by means of stratified random sampling within
325 the training and testing polygons, and the numbers of each LU and LC class were made
326 proportional to the area of the total reference polygons for each class. For classes that were
327 sparsely covered (e.g., railway), their sample sizes were enlarged to achieve a representative
328 distribution. Approximately, 600 and 1000 samples per class for both LU and LC were adopted,
329 allowing the MLP and the CNN networks to be sufficiently trained with a relatively large sample
330 size. These sample points were cross-validated by the Ordnance Survey MasterMap Topographic
331 Layer, Open Street Maps, and the CEH Land Cover® plus: Crops
332 (<https://www.ceh.ac.uk/crops2015>) to ensure precision and the fidelity of the selected samples.

333 3.2 Experimental design and parameters

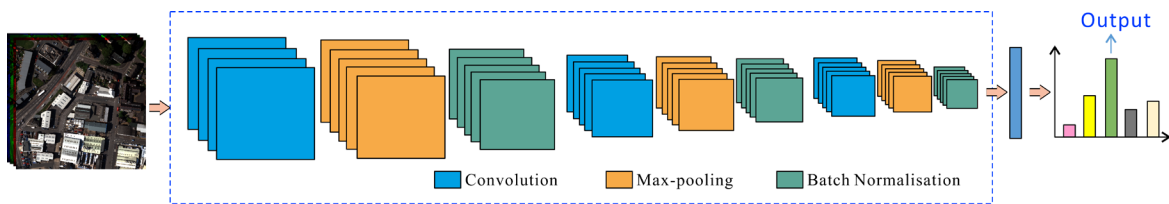
334 Within the SS-JDL method, the MLP and OCNN classifiers need to predefine parameters to
335 obtain the highest classification accuracy and generalisation for both study sites. These models
336 were parameterised in S1 and directly applied to S2, as recommended by Zhang *et al.* (2018c)
337 and Zhang *et al.* (2019). The structures of the model and parameters are detailed below.

338 For MLP, the initial input is four-band image at the pixel level, and the initial prediction of each
339 pixel corresponds to the LC category. Two hidden layers were chosen as optimal with 20 nodes
340 in each layer. The activation functions for the hidden layers were set as ‘Rectified Linear Unit’
341 to achieve nonlinearity within the MLP network, and the number of epochs was tuned to 1000
342 to allow full convergence to a stable state through backpropagation.

343 The OCNN requires pre-processing of the image into homogeneous objects that are
344 representative of specific LCs through object-based image segmentation. Multi-resolution
345 segmentation was implemented using the eCognition 9.2 software to acquire the segmented

346 objects. The scale parameter was varied from 10 to 100 to explore the influence of object size
347 on segmentation performance, and 40 was found to be the optimal parameter to obtain slightly
348 over-segmented results.

349 For each object, a standard CNN was applied to an image patch located at the object centre to
350 learn the within-object information and its spatial context. Nine hidden layers that alternate with
351 convolution, max-pooling, and batch normalisation, were designed to capture the deep LU
352 feature representations (Figure 3). Small filters (3×3) in convolutional layers were adopted
353 following the common deep network structures (e.g., VGG-16), and the number of filters was
354 tuned as 64 to extract the multi-dimensional deep feature representations. The learning rate and
355 the epoch were set as 0.01 and 800, respectively, to learn the deep features through iteration.



356
357 Figure 3. Model structures and architectures of the deep CNN network with nine hidden layers.

358 3.3 Benchmarks and parameter settings

359 In this research, five typical methods served as benchmarks for LC classification, including the
360 MLP (spectral only), GLCM-MLP (spectral and textural features), Markov random field (MRF,
361 contextual-based), Multi-scale CNN applied to land cover (MCNN-LC), and the recently
362 proposed Joint Deep Learning method applied to land cover (JDL-LC; as for SS-JDL but without
363 scale sequencing). As for LU classification, five state-of-the-art approaches were benchmarked,
364 including MRF, object-based image analysis (OBIA), the standard pixel-wise CNN, Multi-scale
365 CNN applied to land use (MCNN-LU), and Joint Deep Learning applied to land use (JDL-LU).
366 The classification experiments were implemented using Keras/Tensorflow under a Python

367 environment using a laptop with a NVIDIA 940M GPU and 12.0 GB memory. The parameters
368 of these benchmark comparators are detailed below.

369 **MLP** took pixel-based four spectral bands as input, with two hidden layers inside the network
370 and 20 nodes for each of them as parameterised by Zhang *et al.* (2018a). The output was the LC
371 label for each pixel.

372 **GLCM-MLP** used the same structure as the MLP, while grey-level co-occurrence matrix
373 (GLCM) texture variables were added as additional input features. The prediction was the LC
374 class label at the pixel level.

375 **MRF** took the support vector machine as its basic spectral classifier for both LU and LC
376 classification, in which the Radial Basis Function was adopted as the kernel function. Following
377 the recommendations of Zhang *et al.* (2018b), the window size of the MRF was tuned as 5×5 ,
378 and the smoothing parameter was set as 0.7 to achieve smoothed results using contextual
379 information.

380 **MCNN** was designed for both land cover (MCNN-LC) and land use (MCNN-LU) classification
381 based on majority voting at three input scales (CNN window sizes) as proposed by Lv *et al.*
382 (2018). Following the recommendation of Lv *et al.* (2018), three CNN window sizes at 15×15 ,
383 25×25 , and 35×35 were used as the input patch sizes to classify regions produced by multi-
384 resolution segmentation with a scale parameter of 20. The predictions of the triple-scale CNNs
385 were fused through majority voting to obtain LC and LU classification results, respectively.

386 **JDL-LC** incorporated an MLP and OCNN to learn iteratively the LU and LC classification
387 probabilities, respectively. The number of iterations was set to 15 to allow full convergence to a
388 stable state. The prediction of the MLP at the final iteration was taken as the JDL-LC
389 classification result (Zhang *et al.*, 2019).

390 **OBIA** was implemented on objects derived from multi-resolution segmentation. Various
391 features were then extracted from the objects, including spectral features (mean and standard
392 deviation), GLCM texture variables and geometry. An SVM was used for object-based
393 classification using these hand-coded features.

394 **CNN** was a trained deep network to predict pixel-wise densely overlapping patches across entire
395 image. The input patch size was parameterised as 48×48 as recommended by Långkvist *et al.*
396 (2016), and the number of layers was set as six (alternating between convolution and max-
397 pooling). Softmax regression was adopted to predict the final LU classification results.

398 **JDL-LU** was performed by a pixel-based MLP to predict LC probabilities which were used as
399 input features for LU prediction using an object-based CNN. This system can jointly learn the
400 LU and LC classes through iteration. The JDL-LU classification result was achieved at 15
401 iterations with a steady state (Zhang *et al.*, 2019).

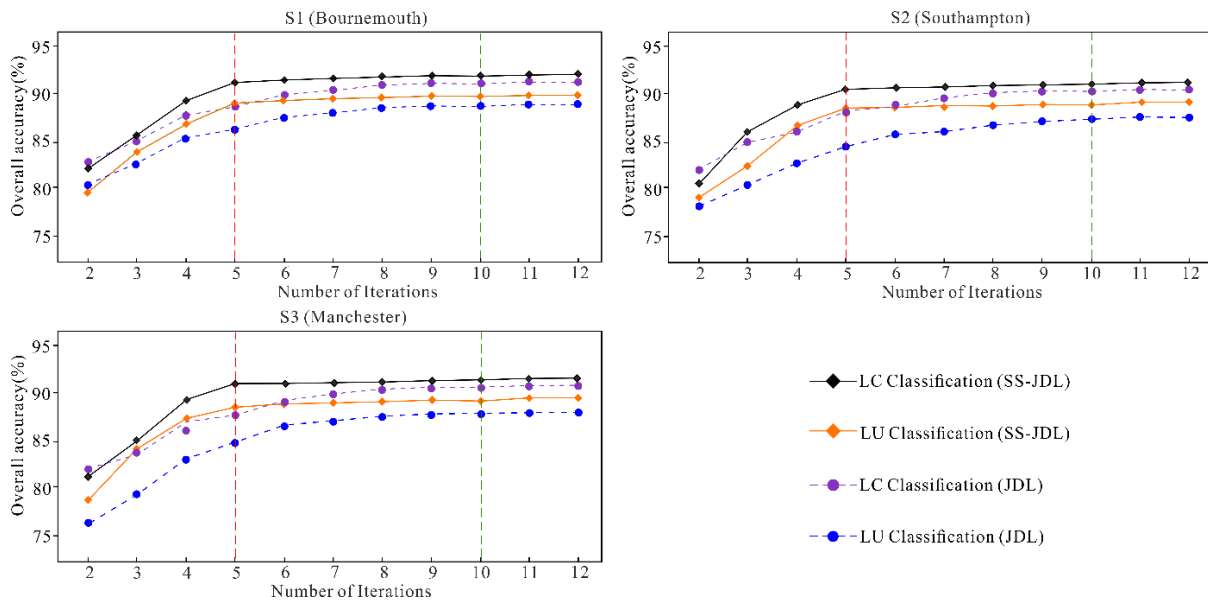
402 3.4 Classification Results and Analysis

403 3.4.1 Results and analysis of the scale sequence

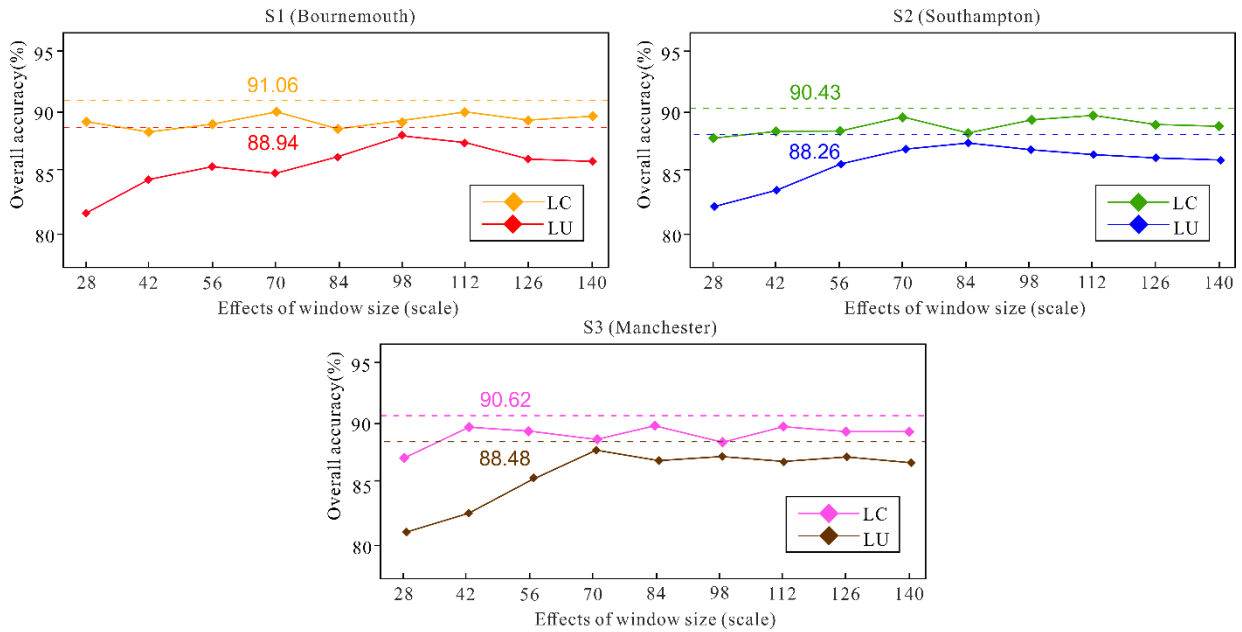
404 The minimum scale for the SS-JDL was set as 28×28 to capture the within-object information,
405 given that the main axis of the smallest object size was found to be less than 14 metres in S1, S2
406 and S3. The maximum scale was parameterised as 140×140 by considering the largest object
407 within the three scenes to cover the wider spatial context while leveraging the representation
408 capability of the CNN network. Between the minimum and maximum scales, a range of scales
409 were interpolated into the network to obtain a sequence of scales (i.e., CNN window sizes). The
410 smallest number of iterations for the SS-JDL was two representing the minimum and maximum
411 scales only. The number of iterations increases as more scales are introduced. Figure 4
412 demonstrates the influence of the number of iterations on the overall accuracy, and the SS-JDL
413 method is compared with the recently proposed JDL method on both the S1 and S2 images

414 through iteration. The SS-JDL method consistently shows rapid convergence, with the optimal
 415 accuracy achieved in just 5 iterations (red dashed line), significantly faster than the JDL method
 416 for both LU and LC classification at 10 iterations (green dashed line). Specifically, for S1, the
 417 SS-JDL accuracy started at around 82% and 79% for the LC and LU classifications at iteration
 418 2, and rapidly increased to approximately 91% (LC) and 88.5% (LU) at iteration 5. In contrast,
 419 the JDL accuracy was slightly higher than that of the SS-JDL at iteration 2, with around 82.5%
 420 (LC) and 80% (LU), and increased slowly towards the optimum accuracy of ~90% (LC) and
 421 ~87% (LU) at iteration 10.

422 A similar trend was found in S2 and S3 (Figure 4), where the SS-JDL accuracy began at around
 423 80% for LC and 79% for LU, and reached 90% (LC) and 88% (LU) at iteration 5. The accuracy
 424 of the JDL-LC classifier was slightly higher at iteration 2 (81%), and gradually increased to
 425 around 89% at iteration 10, which is still lower than that of the LC classification of SS-JDL
 426 (90%). The accuracy of the JDL-LU, in contrast, started lower than that of the SS-JDL, at around
 427 78.5% at iteration 2, and slowly increased with iteration. The optimal accuracy was found at
 428 iteration 10 with around 86% accuracy (2% lower than for the LU classification of SS-JDL).



429
 430 Figure 4. The influence of iteration upon overall accuracy for the LU and LC classifications using the
 431 proposed SS-JDL and the JDL method.



432

433 Figure 5. The effects of window size (scale) on overall accuracy of the LU and LC classifications using
 434 the SS-JDL (dashed lines) and the JDL method (solid lines).

435 The SS-JDL involves multiple scales across the scale sequence and, thus, does not require
 436 optimal scale selection. Figure 5 shows the scale selection processes for JDL in comparison to
 437 the SS-JDL method with 5 iterations (scales). A range of CNN window sizes were considered,
 438 including 28×28 , 42×42 , 56×56 , 70×70 , 84×84 , 98×98 , 112×112 , 126×126 , and 140×140 , and
 439 the classifier at each window size was run 20 times to achieve the converged LU and LC
 440 classification results. As shown in Figure 5, the SS-JDL method (dashed lines) always
 441 outperforms the JDL (solid lines) for both LC classification (OA of 91.06%, 90.43% and 90.62%)
 442 and LU classification (OA of 88.94%, 88.26% and 88.48%) for S1, S2 and S3, respectively. For
 443 JDL, both LU and LC classifications demonstrate variation along the changing window size, and
 444 it is hard to judge the optimal scale. In S1, 28×28 , 70×70 and 112×112 are potentially the
 445 “optimal” LC window size, whereas the optimal scale for LU classification might be 98×98 .
 446 Likewise, for S2 multiple accuracy peaks are produced for LC (70×70 , 112×112 , 140×140),
 447 while a single optimum scale (84×84) is found for LU. Similar trends are found in S3, with three
 448 accuracy peaks for LC (42×42 , 84×84 , 112×112) and one optimum scale (70×70) for LU. Clearly,

449 the LU classification is much more sensitive to scale effects with larger accuracy differences
450 (around 81% to 88%), whereas the LC classification does not have as clear a correlation to the
451 CNN window size. In addition, the “optimal” scales for LU and LC are completely different. For
452 example, the optimal scale for LU in S1 is found at 98×98, but this does not coincide with the
453 optimal scales for LC (28×28, 70×70 and 112×112). The SS-JDL, therefore, demonstrates
454 greater classification accuracy for all study sites (S1, S2 and S3) without requiring an optimal
455 scale selection process.

456 In this paper, a forward scale sequence (FSS) derived by the minimum and the maximum sizes
457 of the segmented objects in the imagery was adopted for JDL classification. The potential
458 sampling space for the scale sequences, however, is enormous (from completely random to
459 sequential scales), and it is extremely hard to examine exhaustively the entire set of possible
460 scale choices. To better explore the space, four typical sampling schemes were considered,
461 including the forward scale sequence (FSS) from small to large scale, the backward scale
462 sequence (BSS) from large to small scale, the random scale sequence (RSS) with scales in a
463 completely random order generated by a Monte Carlo method, as well as the iterative greedy
464 scale sequence (IGSS) that chooses the scale with the best accuracy increase at each iteration.
465 Table 2 demonstrates the superiority of FSS in OA and computational efficiency compared with
466 IGSS, RSS, and BSS. The high OA is achieved by gradually enlarging the observational scales
467 from the minimum to the maximum, while retaining the precise information achieved initially at
468 the smaller scales through subsequent scales. In the meantime, exhaustive search (e.g., IGSS)
469 was not required by the FSS, thereby significantly reducing the computational time through fast
470 implementation.

471 Table 2. The overall accuracy and the computational time of four sampling schemes, including forward
472 scale sequence (FSS), backward scale sequence (BSS), random scale sequence (RSS), and iterative
473 greedy scale sequence (IGSS).

| Sampling scheme | Overall Accuracy (%) | | | Computational time (h) |
|-----------------|----------------------|--------------|--------------|------------------------|
| | S1 (LC, LU) | S2 (LC, LU) | S3 (LC, LU) | S1, S2, S3 |
| FSS | 91.06, 88.94 | 90.43, 88.26 | 90.62, 88.48 | 7.52, 7.86, 7.32 |
| BSS | 86.73, 83.84 | 86.68, 83.05 | 87.04, 84.26 | 7.52, 7.86, 7.64 |
| RSS | 87.24, 84.32 | 87.59, 84.13 | 87.74, 83.85 | 8.95, 9.37, 9.28 |
| IGSS | 90.35, 87.69 | 89.76, 87.14 | 89.43, 87.25 | 35.58, 37.94, 36.65 |

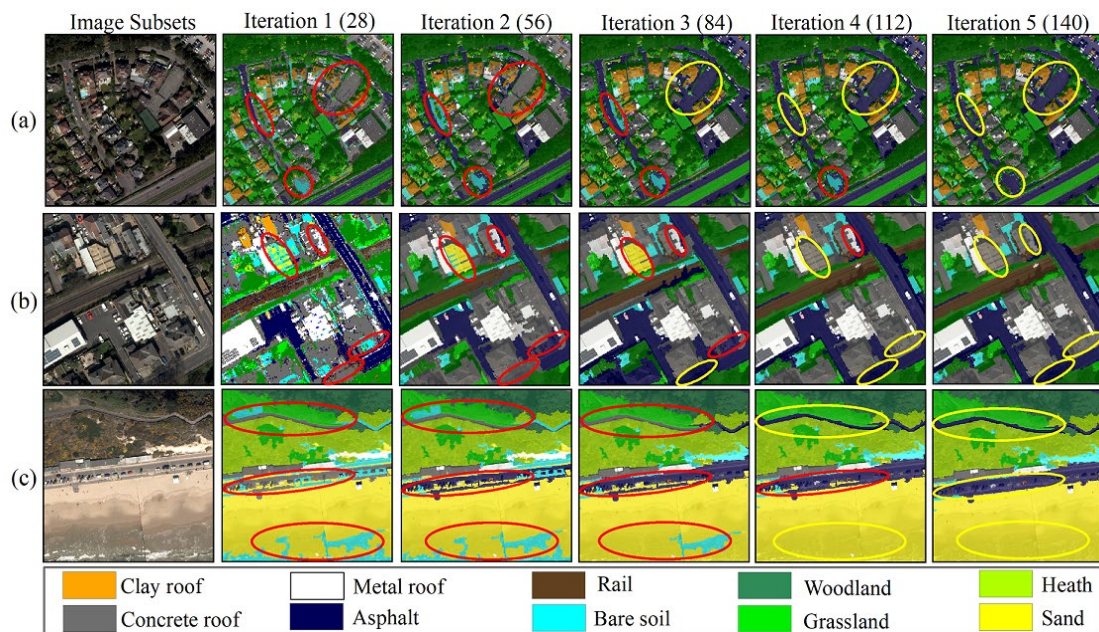
474

475 3.4.2 Classification results and analysis for all study sites

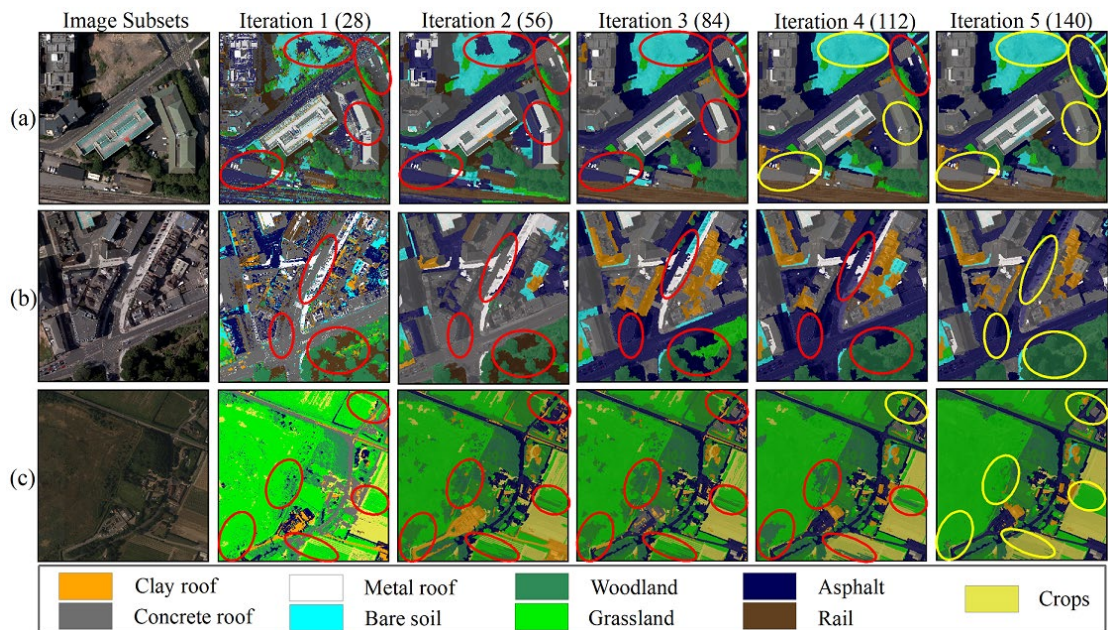
476 To gain a better spatial visualisation of how the classification accuracy increases with iteration,
 477 the converged five iterations of the SS-JDL for both LC (Figure 6, 7 and 8) and LU (Figure 9,
 478 10 and 11) are demonstrated at iteration 1 (28×28) to iteration 5 (140×140) using three subsets
 479 of S1 and S2 as well as one subset of S3, respectively (Figures 6 to 11).

480 The LC classification result at iteration 1 (28×28) contained severe salt-and-pepper effects, as
 481 shown in Figure 6 (a, b and c), Figure 7 (a, b and c), and Figure 8(b). Such problems were tackled
 482 through iteration by incorporating spatial context from the LU probabilities and increasing the
 483 scale at each iteration. Iteration 2 significantly smoothed the classification results while keeping
 484 the fidelity in the representations, thereby enhancing the classification accuracy, accordingly.
 485 Figure 6(b) illustrates the clear increase in accuracy achieved by reducing the noise (salt-and-
 486 pepper effects) in the Asphalt road and the Rail classes as well as the Concrete roof class. Both
 487 iterations 1 and 2, however, failed to differentiate Concrete roof and Asphalt (e.g., the red circles
 488 in Figure 6(a) and 6(c) as well as Figure 7(b)), given the extremely similar spectral reflectance
 489 between them. Those pixels misclassified as Concrete roof were rectified to Asphalt after
 490 iteration 3 and remained the same throughout further iterations (e.g. Figure 8(c)). Another
 491 remarkable improvement demonstrated through iteration was the elimination of Bare soil within
 492 the classification maps. For example, the falsely classified Bare soil pixels at iterations 1 to 4 of
 493 Figure 6(a) and iterations 1 to 3 of Figure 6(c) were corrected as Asphalt and Sand, respectively.

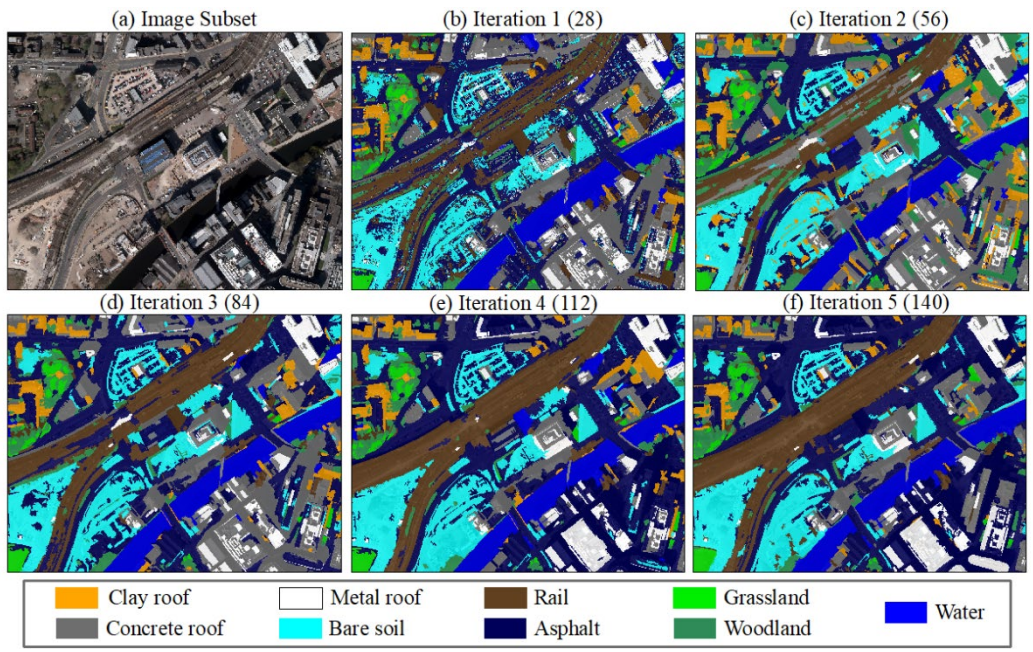
494 More impressively, the shadow effects cast by the woodland and buildings shown in Figure 7(b)
 495 and Figure 8(a) were falsely classified as Rail and Concrete roof at iterations 1 and 2, but were
 496 gradually rectified to Asphalt or partial Woodland at iterations 3 and 4, and the shadow adjacent
 497 to the trees was completely replaced as entirely Woodland at iteration 5. In terms of agricultural
 498 land, the Crop and Grassland classes were more clearly differentiated through further iteration.
 499 Figure 7(c) demonstrates the misclassified Grassland at iterations 1, 2 and 3, which was partially
 500 rectified to Crops at iteration 4, and completely identified as Crops with high accuracy at iteration
 501 5.



502
 503 Figure 6. Three subset (i.e., a, b, c) of LC classification in S1 using Scale Sequence Joint Deep
 504 Learning (SS-JDL) from iteration 1 (28×28) to 5 (140×140). The correct and incorrect classifications
 505 are highlighted by circles in yellow and red, respectively.



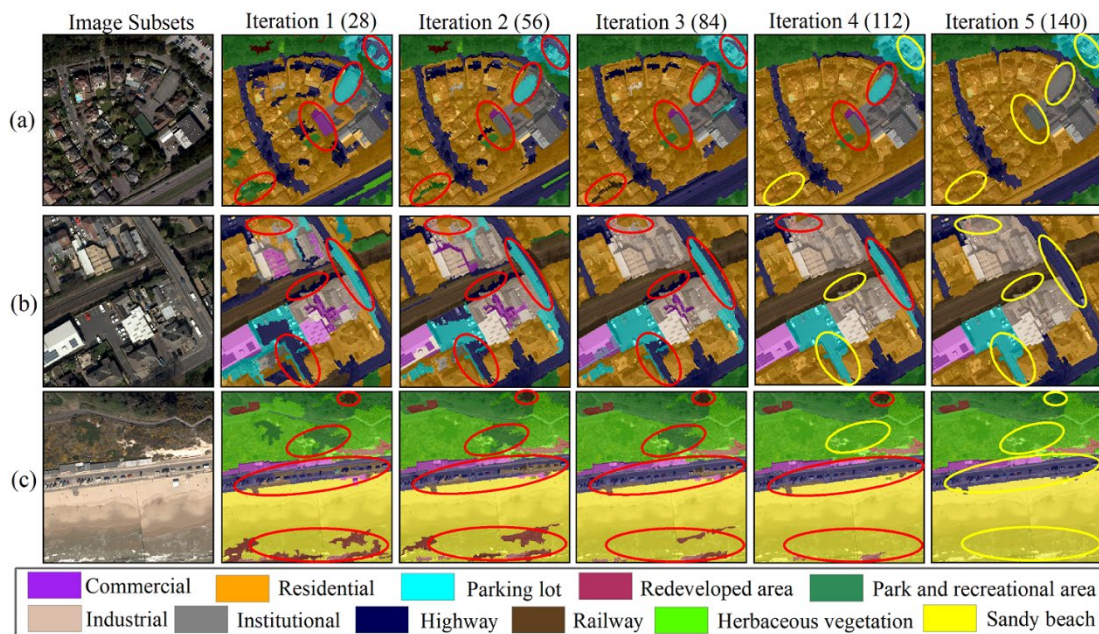
506
 507 Figure 7. Three subset (i.e., a, b, c) of LC classification in S2 using Scale Sequence Joint Deep
 508 Learning (SS-JDL) from iteration 1 (28×28) to 5 (140×140). The correct and incorrect classifications
 509 are highlighted by circles in yellow and red, respectively.



510
 511 Figure 8. The land cover classification in S3 using Scale Sequence Joint Deep Learning (SS-JDL) from
 512 iteration 1 (28×28) to 5 (140×140).

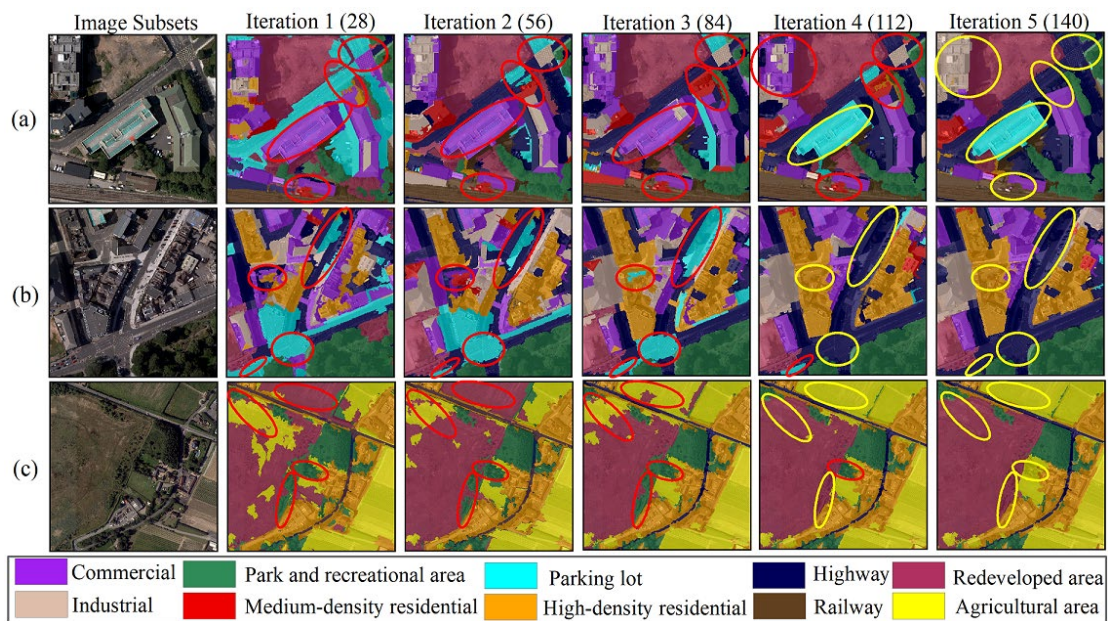
513 In terms of LU classification, the most significant increase in accuracy was obtained for the
 514 Parking lot class, which was correctly differentiated after iteration. For example, the confusion

515 between Parking lot and Highway is shown in Figure 9(b) at iterations 1 to 4 and Figure 10(b)
 516 at iterations 1 to 3 (red circles) and Figure 11(b) and 11(c), which was resolved and clearly
 517 identified as Highway at iteration 5 (yellow circles). Those pixels misclassified as Commercial
 518 at iterations 1 to 3 (Figure 10(a)) were correctly modified to Parking lot at iterations 4 and 5.
 519 Furthermore, the misclassification between Highway and Railway was rectified throughout the
 520 iterative process. For example, Figure 9(b) and 11(d) show that some Railways were affected by
 521 shadows and wrongly identified as Highway at iterations 1 to 3. Likewise, some of the Highways
 522 in Figure 9(c) were falsely classified as Railway at iterations 1 to 4 when adjacent to sandy
 523 beaches. These problems were addressed and differentiated accurately at iteration 5 in all cases.
 524 Moreover, the mutual confusion between Agricultural area and Redeveloped area is shown in
 525 Figure 10(c) with red circles, which was precisely distinguished with sharp boundaries at the 5th
 526 iteration (in yellow circles).



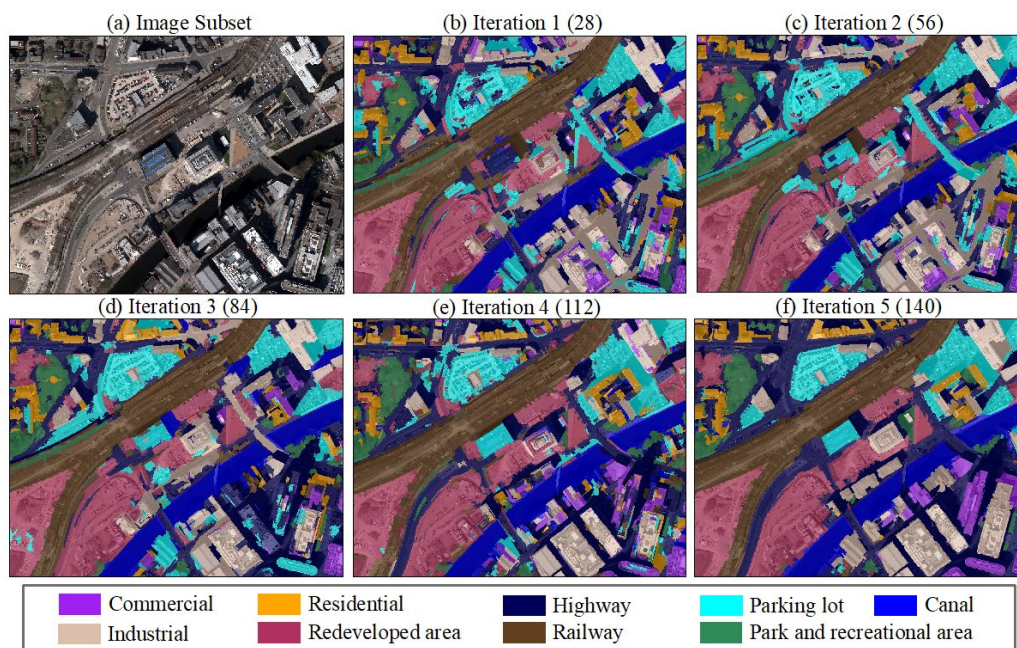
528 Figure 9. Three subset (i.e., a, b, c) of LU classification in S1 using Scale Sequence Joint Deep
 529 Learning (SS-JDL) from iteration 1 (28×28) to 5 (140×140). The correct and incorrect classifications
 530 are highlighted by circles in yellow and red, respectively.

531



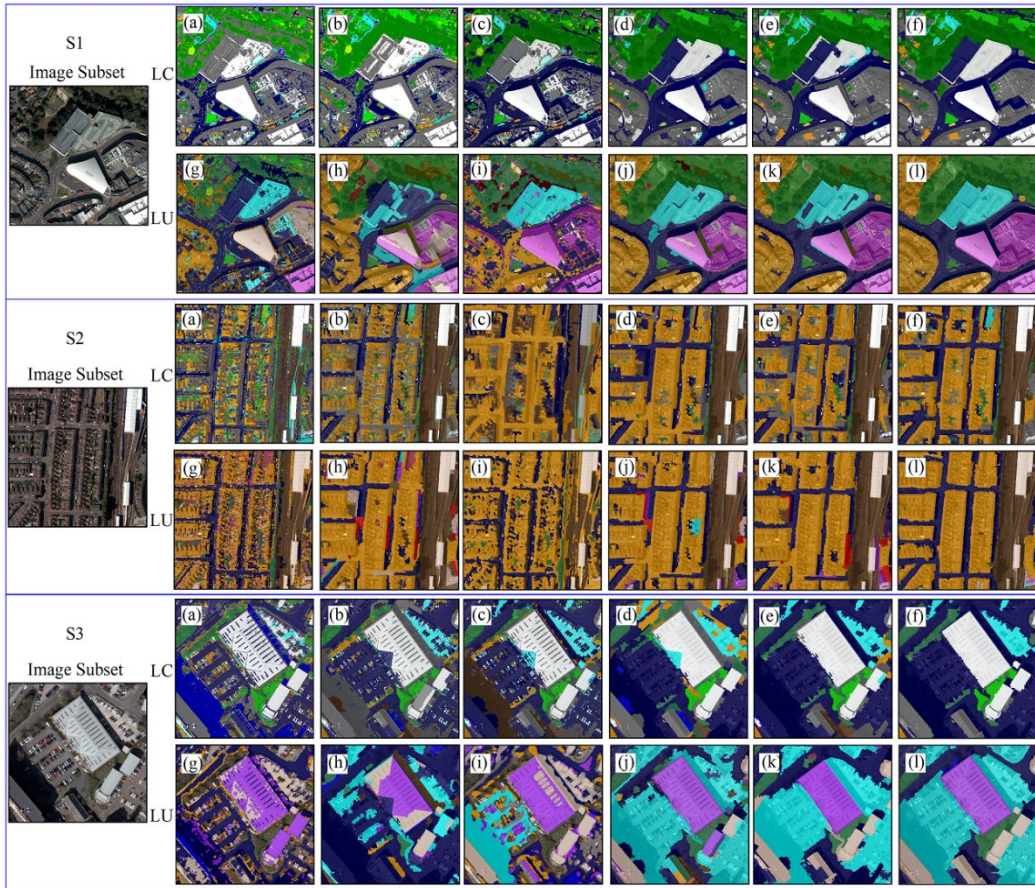
532

533 Figure 10. Three subset (i.e., a, b, c) of LU classification in S2 using Scale Sequence Joint Deep
 534 Learning (SS-JDL) from iteration 1 (28×28) to 5 (140×140). The correct and incorrect classifications
 535 are highlighted by circles in yellow and red, respectively.



536

537 Figure 11. The land use classification in S3 using Scale Sequence Joint Deep Learning (SS-JDL) from
 538 iteration 1 (28×28) to 5 (140×140).



539
 540 Figure 12. Image subset benchmark comparison among various methods for S1, S2 and S3. The LC
 541 classifications include (a) MLP, (b) GLCM-MLP, (c) MRF, (d) MCNN-LC, (e) JDL-LC, and the (f)
 542 SS-JDL-LC. The LU classifications include (g) MRF, (h) OBIA, (i) CNN, (j) MCNN -LU, (k) JDL-LU,
 543 and the (l) SS-JDL-LU. Refer to Figures 6 to 11 for details of the corresponding classification legends.

544 The classification accuracy of the proposed SS-JDL was further compared with a range of
 545 benchmark approaches for S1, S2 and S3, respectively. The LC results (SS-JDL-LC) were
 546 benchmarked with other comparators, including the MLP, the GLCM-MLP, the MRF, the
 547 MCNN-LC, and the JDL-LC; whereas, the LU results (SS-JDL-LU), were compared with MRF,
 548 OBIA, CNN, MCNN-LU, and the JDL-LU. Visual inspections and accuracy assessment, based
 549 on the overall accuracy (OA), Kappa coefficient (κ) and the per-class mapping accuracy, were
 550 used to test the classification results.

551 Figure 12 demonstrates visually the classification results of S1, S2 and S3 amongst the various
 552 benchmark methods. For LC, the pixel-based MLP showed the lowest classification accuracy

553 due to the severe salt-and-pepper effects in all study sites (Figure 12(a)). Confusion was found
554 between the Asphalt and Concrete roof classes together with the severe issues of shadow cast by
555 buildings and woodlands. The GLCM-MLP incorporated spatial texture within the image, which
556 increased the capability to capture ground objects with distinctive textures. For example, the
557 woodlands with coarse textures were identified accurately in Figure 12(b). Such GLCM-MLP
558 based classification results, however, still suffered from difficulties in differentiating those LC
559 classes with similar spectra and textures (e.g., the Asphalt and Concrete roof classes). The MRF
560 significantly increased the ability to characterise the Asphalt road class by borrowing adjacent
561 neighbourhood information, but suffered from some issues with respect to other classes (e.g.,
562 Concrete roof and Clay roof) as illustrated in Figure 12(c). The MCNN-LC clearly showed
563 increased accuracy in differentiating Asphalt and Concrete roof, but some edges along the roads
564 and bare soils were misclassified as Clay roof (Figure 12(d)). The JDL-LC significantly
565 increased the classification accuracy using LU and LC characteristics iteratively (Figure 12(e)).
566 It, however, failed to resolve some problems along the object boundaries (e.g., for the Asphalt
567 class). The proposed SS-JDL-LC method solved all these problems achieving a high accuracy
568 overall (Figure 12(f)).

569 In terms of LU classification, the MRF demonstrated serious deficiencies in identifying
570 residential and commercial areas with noisy results (Figure 12(g)). OBIA smoothed the LU
571 classification to a large extent, but failed to differentiate complex objects such as the Parking lot
572 and Industrial classes, and lost some fine-grained details (e.g., Highway) (Figure 12(h)). The
573 pixel-wise CNN showed some advantages in capturing complex LU classes (e.g., Parking lot,
574 Commercial). It, however, produced severe geometric distortions (e.g., the enlarged commercial
575 buildings) and poorly defined boundaries (e.g., the edge between the Residential and Highway
576 classes) (Figure 12(i)). The MCNN-LU achieved increased accuracy in classifying the Parking
577 lot class, but failed to capture continuous linear features such as Highway or Railway (Figure

578 12(j)). JDL-LU (Figure 12(k)) and the proposed SS-JDL-LU (Figure 12(l)) share similar
579 classification results with high precision and fidelity. The SS-JDL-LU, surprisingly,
580 demonstrated some further improvements in identifying detailed objects and their boundaries
581 (e.g., Highway).

582 The quantitative accuracy assessment for LC classification is reported in Tables 3, 4 and 5 for
583 S1, S2 and S3, respectively. The SS-JDL-LC consistently achieved the highest OA of 91.06%,
584 90.43% and 90.62% ($\kappa = 0.90, 0.89$ and 0.89) for S1, S2 and S3, respectively, greater than the
585 JDL-LC of 89.68%, 88.29% and 88.48% ($\kappa = 0.88, 0.87$ and 0.87), the MCNN-LC of 87.54%,
586 86.95% and 86.57% ($\kappa = 0.86, 0.86$ and 0.85), the MRF of 84.32%, 84.78% and 84.54% ($\kappa =$
587 $0.84, 0.84$ and 0.83), the GLCM-MLP of 83.24%, 82.85% and 83.06% ($\kappa = 0.82, 0.82$ and 0.82),
588 and the MLP of 82.06%, 81.29% and 82.22% ($\kappa = 0.81, 0.80$ and 0.81), respectively. In terms of
589 LU classification, the SS-JDL-LU yielded the greatest OA (88.94%, 88.26% and 88.48%) for
590 S1, S2 and S3 with the highest κ (0.89, 0.88 and 0.88), consistently higher than the JDL-LU (OA
591 = 87.68%, 87.58% and 86.26%, $\kappa = 0.88, 0.87$ and 0.86), the MCNN-LU (OA = 85.94%, 85.29%
592 and 85.08%, $\kappa = 0.86, 0.85$ and 0.84), the CNN (84.32%, 84.08% and 83.32%, $\kappa = 0.84, 0.83$
593 and 0.82), the OBIA of (82.17%, 80.26% and 80.42%, $\kappa = 0.82, 0.80$ and 0.80), and the MRF
594 (81.06%, 79.38% and 79.29%, $\kappa = 0.80, 0.79$ and 0.79).

595 The per-class mapping accuracy further demonstrated the superiority of the SS-JDL method,
596 with the most accurate results shown in bold font in Tables 3 to 8. Specifically, for LC
597 classification, the Clay roof, Metal roof, Woodland, Grassland, Asphalt classes were accurately
598 classified in S1, S2 and S3 using the SS-JDL-LC (accuracy > 90%) by incorporating spatial and
599 spectral feature representations across different scales. Such high accuracies were also achieved
600 for Heath (90.07%) and Sand (92.62%) in S1, Crops (90.74%) in S2 and Water (98.27%) in S3.
601 The accuracies of these LC classes, in particular Woodland and Grassland (90.99% and 91.62%
602 on average), were significantly higher than for the benchmarks, with average accuracies for the

603 MLP (69.36% and 71.74%), GLCM-MLP (72.78% and 71.63%), MRF (76.15% and 75.47%),
604 MCNN-LC (85.95% and 86.05%), and JDL-LC (88.75% and 90.35%), respectively. The
605 Concrete roof class was the most challenging LC class to be classified, producing the lowest
606 accuracy of 83.07% on average for the SS-JDL-LC, which was nevertheless significantly higher
607 than for the MLP (70.19%), GLCM-MLP (72.62%), MRF (73.89%), MCNN-LC (77.56%), and
608 JDL-LC (79.56%), respectively. Accuracies for other classes, such as Rail and Bare soil (88.57%
609 and 87.16%) were less significantly increased using the SS-JDL-LC compared with the
610 benchmark methods, in which less than 5% accuracy differences were found among them.

611 Tables 6, 7 and 8 show the quantitative accuracy assessment for LU classification for S1, S2 and
612 S3, respectively. The greatest accuracy increases were shown for the Commercial, Industrial,
613 Parking lot and Highway classes, with average accuracies of 85.10%, 85.58%, 91.71%, and
614 84.74%, respectively, for the proposed SS-JDL-LU, much higher than for the MRF (70.75%,
615 70.78%, 79.12%, 78.37%), OBIA (71.24%, 71.06%, 81.42%, 78.85%), CNN (73.85%, 73.64%,
616 84.16%, 79.10%), MCNN-LU (78.19%, 80.14%, 86.20%, 80.44%), and JDL-LU (82.61%,
617 83.74%, 88.08%, 81.57%). For the Residential, Redeveloped area, and Park and recreational area
618 classes, moderately increased accuracies were obtained by the SS-JDL-LU (88.49%, 91.59%,
619 and 95.02%), greater than for the MRF (80.27%, 81.74%, 88.29%), OBIA (81.39%, 83.79%,
620 90.06%), CNN (82.06%, 86.79%, 91.29%), MCNN-LU (83.86%, 88.24%, 91.42%), and JDL-
621 LU (86.63%, 89.70%, 93.69%), respectively. Other LU classes, including Railway, Herbaceous
622 vegetation, Sandy beach, Canal, and Agricultural area, did not show significant increases in
623 accuracy in comparison with the benchmarks, with similar accuracies being achieved by the
624 JDL-LU and SS-JDL-LU classifiers.

625 Table 3. LC accuracy comparison for each class and overall between MLP, GLCM-MLP, MRF, MCNN-
626 LC, JDL-LC, and the proposed SS-JDL-LC method in S1. The largest classification accuracies and Kappa
627 coefficients are shown in bold font.

| LC Class (S1) | MLP | GLCM-MLP | MRF | MCNN-LC | JDL-LC | SS-JDL-LC |
|--------------------------------|--------|----------|--------|---------|--------|---------------|
| Clay roof | 90.12% | 88.62% | 89.58% | 88.27% | 91.87% | 92.16% |
| Concrete roof | 70.54% | 73.95% | 74.23% | 77.59% | 80.25% | 84.05% |
| Metal roof | 90.17% | 90.28% | 90.16% | 90.82% | 91.34% | 91.64% |
| Woodland | 69.45% | 73.02% | 76.28% | 85.43% | 88.24% | 90.82% |
| Grassland | 72.36% | 72.94% | 75.53% | 86.32% | 90.65% | 92.43% |
| Asphalt | 89.42% | 88.57% | 89.42% | 88.29% | 90.22% | 90.68% |
| Rail | 83.21% | 83.26% | 83.56% | 86.37% | 88.54% | 88.95% |
| Bare soil | 80.23% | 81.05% | 82.44% | 83.52% | 85.59% | 86.78% |
| Heath | 82.63% | 83.84% | 86.18% | 87.24% | 89.74% | 90.07% |
| Sand | 88.39% | 88.98% | 89.54% | 89.43% | 91.42% | 92.62% |
| Overall Accuracy (OA) | 82.06% | 83.24% | 84.32% | 87.54% | 89.68% | 91.06% |
| Kappa Coefficient (κ) | 0.81 | 0.82 | 0.84 | 0.86 | 0.88 | 0.90 |

628 Table 4. LC accuracy comparison for each class and overall between MLP, GLCM-MLP, MRF, MCNN-
629 LC, JDL-LC, and the proposed SS-JDL-LC method in S2. The largest classification accuracies and Kappa
630 coefficients are shown in bold font.

| LC Class (S2) | MLP | GLCM-MLP | MRF | MCNN-LC | JDL-LC | SS-JDL-LC |
|--------------------------------|--------|----------|--------|---------|--------|---------------|
| Clay roof | 89.57% | 88.27% | 89.17% | 90.05% | 91.36% | 91.92% |
| Concrete roof | 69.45% | 71.82% | 73.24% | 77.56% | 79.48% | 82.43% |
| Metal roof | 89.36% | 89.43% | 90.18% | 90.74% | 91.56% | 91.86% |
| Woodland | 69.03% | 72.18% | 76.84% | 86.39% | 88.54% | 90.74% |
| Grassland | 70.64% | 71.36% | 75.42% | 84.28% | 90.06% | 91.87% |
| Asphalt | 88.42% | 88.75% | 89.43% | 88.62% | 87.64% | 90.22% |
| Rail | 82.06% | 82.64% | 83.57% | 85.34% | 87.25% | 88.16% |
| Bare soil | 80.12% | 80.92% | 82.45% | 83.27% | 85.74% | 87.23% |
| Crops | 84.15% | 85.28% | 86.58% | 88.21% | 89.63% | 90.74% |
| Overall Accuracy (OA) | 81.29% | 82.85% | 84.78% | 86.95% | 88.29% | 90.43% |
| Kappa Coefficient (κ) | 0.80 | 0.82 | 0.84 | 0.86 | 0.87 | 0.89 |

631 Table 5. LC accuracy comparison for each class and overall between MLP, GLCM-MLP, MRF, MCNN-
632 LC, JDL-LC, and the proposed SS-JDL-LC method in S3. The largest classification accuracies and Kappa
633 coefficients are shown in bold font.

| LC Class (S3) | MLP | GLCM-MLP | MRF | MCNN-LC | JDL-LC | SS-JDL-LC |
|--------------------------------|--------|----------|--------|---------|--------|---------------|
| Clay roof | 90.06% | 87.45% | 89.55% | 90.05% | 90.82% | 91.35% |
| Concrete roof | 70.58% | 72.08% | 74.21% | 77.53% | 78.96% | 82.74% |
| Metal roof | 90.12% | 88.36% | 90.09% | 90.19% | 90.88% | 91.28% |
| Woodland | 69.59% | 73.14% | 75.32% | 86.02% | 89.47% | 91.42% |
| Grassland | 72.22% | 70.59% | 75.45% | 87.54% | 90.35% | 90.56% |
| Asphalt | 89.46% | 88.62% | 89.42% | 88.57% | 88.24% | 90.73% |
| Rail | 83.18% | 83.42% | 84.36% | 85.42% | 87.89% | 88.59% |
| Bare soil | 80.21% | 80.75% | 82.25% | 82.76% | 84.92% | 87.46% |
| Water | 97.54% | 96.28% | 97.43% | 96.53% | 98.06% | 98.27% |
| Overall Accuracy (OA) | 82.22% | 83.06% | 84.54% | 86.57% | 88.48% | 90.62% |
| Kappa Coefficient (κ) | 0.81 | 0.82 | 0.83 | 0.85 | 0.87 | 0.89 |

634 Table 6. LU accuracy comparison for each class and overall between MRF, OBIA, Pixel-wise CNN,
635 MCNN-LU, JDL-LU, and the proposed SS-JDL-LU method in S1. The largest classification accuracies
636 and Kappa coefficients are shown in bold font.

| LU Class (S1) | MRF | OBIA | CNN | MCNN-LU | JDL-LU | SS-JDL-LU |
|----------------------------|--------|--------|--------|---------|--------|---------------|
| Commercial | 71.11% | 68.47% | 74.16% | 78.52% | 82.72% | 85.95% |
| Industrial | 72.52% | 72.05% | 74.84% | 79.68% | 83.26% | 85.73% |
| Residential | 78.41% | 80.38% | 82.45% | 84.02% | 86.56% | 88.26% |
| Redeveloped area | 82.57% | 84.15% | 87.04% | 88.96% | 90.75% | 92.84% |
| Park and recreational area | 88.42% | 89.54% | 90.76% | 90.47% | 94.59% | 96.59% |
| Parking lot | 79.63% | 82.06% | 84.37% | 86.58% | 88.02% | 92.58% |
| Highway | 81.43% | 79.26% | 80.59% | 83.04% | 84.37% | 88.29% |
| Railway | 85.94% | 88.14% | 88.32% | 89.54% | 91.48% | 91.89% |
| Herbaceous vegetation | 82.71% | 84.37% | 85.24% | 86.82% | 88.57% | 89.02% |

| | | | | | | |
|--------------------------------|--------|--------|--------|--------|--------|---------------|
| Sandy beach | 85.63% | 88.28% | 87.18% | 88.25% | 90.74% | 91.45% |
| Overall Accuracy (OA) | 82.06% | 82.17% | 84.32% | 85.94% | 87.68% | 88.94% |
| Kappa Coefficient (κ) | 0.80 | 0.81 | 0.84 | 0.86 | 0.88 | 0.89 |

637 Table 7. LU accuracy comparison for each class and overall between MRF, OBIA, Pixel-wise CNN,
638 MCNN-LU, JDL-LU, and the proposed SS-JDL-LU method in S2. The largest classification accuracies
639 and Kappa coefficients are shown in bold font.

| LU Class (S2) | MRF | OBIA | CNN | MCNN-LU | JDL-LU | SS-JDL-LU |
|--------------------------------|--------|--------|--------|---------|--------|---------------|
| Commercial | 70.07% | 72.83% | 73.25% | 77.62% | 82.43% | 84.76% |
| Industrial | 67.26% | 69.04% | 71.22% | 80.14% | 84.74% | 85.28% |
| High-density residential | 81.55% | 80.37% | 80.04% | 82.32% | 86.46% | 88.32% |
| Medium-density residential | 82.72% | 84.38% | 85.23% | 86.75% | 88.58% | 88.62% |
| Park and recreational area | 88.02% | 91.12% | 92.34% | 92.74% | 93.06% | 94.02% |
| Parking lot | 78.04% | 80.12% | 83.75% | 85.29% | 88.14% | 91.78% |
| Highway | 77.24% | 78.06% | 76.15% | 77.84% | 79.65% | 82.37% |
| Railway | 88.05% | 90.63% | 86.53% | 89.02% | 91.89% | 91.92% |
| Agricultural area | 85.08% | 88.55% | 87.43% | 88.36% | 90.94% | 91.85% |
| Redeveloped area | 80.08% | 83.07% | 86.24% | 87.82% | 88.62% | 90.69% |
| Overall Accuracy (OA) | 79.38% | 80.26% | 84.08% | 85.29% | 87.58% | 88.26% |
| Kappa Coefficient (κ) | 0.79 | 0.80 | 0.83 | 0.85 | 0.87 | 0.88 |

640 Table 8. LU accuracy comparison for each class and overall between MRF, OBIA, Pixel-wise CNN,
641 MCNN-LU, JDL-LU, and the proposed SS-JDL-LU method in S3. The largest classification accuracies
642 and Kappa coefficients are shown in bold font.

| LU Class (S3) | MRF | OBIA | CNN | MCNN-LU | JDL-LU | SS-JDL-LU |
|----------------------------|--------|--------|--------|---------|--------|---------------|
| Commercial | 71.08% | 72.43% | 74.13% | 78.44% | 82.67% | 84.58% |
| Industrial | 72.57% | 72.08% | 74.85% | 80.59% | 83.22% | 85.73% |
| Residential | 78.39% | 80.42% | 80.52% | 82.36% | 84.91% | 88.76% |
| Park and recreational area | 88.43% | 89.52% | 90.78% | 91.05% | 93.43% | 94.47% |

| | | | | | | |
|--------------------------------|--------|--------|--------|--------|--------|---------------|
| Parking lot | 79.68% | 82.05% | 84.36% | 86.74% | 88.09% | 90.92% |
| Highway | 76.43% | 79.22% | 80.57% | 80.43% | 82.02% | 83.59% |
| Railway | 85.96% | 88.17% | 88.31% | 89.15% | 90.39% | 91.65% |
| Redeveloped area | 82.57% | 84.14% | 87.09% | 87.95% | 89.72% | 91.24% |
| Canal | 90.68% | 92.27% | 94.16% | 95.48% | 96.58% | 96.84% |
| Overall Accuracy (OA) | 79.29% | 80.42% | 83.32% | 85.08% | 86.26% | 88.48% |
| Kappa Coefficient (κ) | 0.79 | 0.80 | 0.82 | 0.84 | 0.86 | 0.88 |

643

644 **4 Discussion**

645 Spatial scale is a fundamental concern in remotely sensed feature representations, as real-world
646 features are often manifested over a range of scales (e.g., small football pitch and large-scale
647 shopping centres). The importance of scale is well recognised in the remote sensing community
648 through hand-coded and learnt features (e.g., Chen and Tian, 2015; Zhao *et al.*, 2016). However,
649 the current need for scale selection and multi-scale representations are cumbersome and
650 extremely inefficient, and often fail to capture the scale variations of objects and their local and
651 global stationary characteristics. Such issues are crucial for deep learning methods that require a
652 large amount of effort for parameterisation, such as choosing the optimal scale or multiple scales
653 as CNN input window sizes for feature representations. These hyper-parameters within the deep
654 networks are extremely difficult to tune effectively, which severely restricts their practical utility
655 in remotely sensed image classification. To overcome these issues, a scale sequence joint deep
656 learning (SS-JDL) method was developed to solve the complex LU and LC classification
657 problem in an efficient and effective manner.

658 Scale sequence joint deep learning (SS-JDL) provides a novel paradigm that embeds multiple
659 scales explicitly within joint deep learning across different classification hierarchies (e.g., LU
660 and LC). Two major characteristics of SS-JDL include (1) information pathways from small to

661 large scales by mimicking the human visual cognition system, and (2) integrated hierarchical
662 learning between a pixel-based MLP and patch-based CNN across multiple scales.

663 Regarding the former, a forward scale sequence (FSS) was autonomously derived based on the
664 minimum and maximum sizes of objects found within the remotely sensed images to be
665 classified. The FSS represents a sequential observation and identification process from small
666 scale features to large scale contexts and from LC states to LU representations, which is
667 consistent with human visual cognition from simple parts and components towards more
668 generalised and complex concepts as well as higher-level characteristics (Lappe *et al.*, 2013).

669 With the scale sequence, the SS-JDL intrinsically involves multi-scale representations, where
670 input patch sizes for the CNNs change from small to large along the iteration sequence to capture
671 the scale effects manifest in high-order LU features. In contrast, the recently proposed JDL
672 requires a pre-defined CNN window size to be found. This may require experimenting with a
673 wide range of window sizes, to find the potentially “optimal” scale for both LU and LC
674 representations. The entire process of scale selection takes potentially an extremely long time
675 (20 JDL iterations at each scale), and it is impossible to fit a single “optimal” scale for LU and
676 LC simultaneously as shown in Figure 5. Whereas the SS-JDL does not aim to find such an
677 “optimal” scale, but integrates multiple scales through an iterative classification process to
678 represent the scale effects across the scene. For the three study sites, the SS-JDL converged to
679 the optimal solution rapidly (just five iterations or input scales; Figure 4), Thus, five scales are
680 recommended as the default settings for the scale sequence depending on the complexity of the
681 landscape. Within each iteration, the CNN networks learn the LU representations in deep and
682 abstract levels (nine layers in the experiments), which captures the spatial pattern successively
683 in a hierarchy at a specific scale, and continuously learns along the sequence of scales through
684 the iterative process. Such a scale sequence needs only the minimum and the maximum scales,
685 and autonomously interpolates the scale at each iteration, which is simple to implement for

686 practitioners and end-users. Therefore, the proposed SS-JDL is highly suitable for remotely
687 sensed image classification due to its simplicity and effectiveness.

688 For the latter hierarchical learning issue, the complex LU and LC classification problems were
689 addressed jointly through iteration, where the pixel-based MLP and patch-based CNN were
690 integrated through a hierarchy in a way that is mutually beneficial (Zhang *et al.*, 2019).
691 Specifically, at each iteration, the spectral-based MLP was fitted to predict the LC at the pixel
692 level, and based on this, the CNN was applied at the patch level to predict the LU of objects
693 through spatial feature representations. Such joint learning was able to model the hierarchical
694 relations between LU and LC iteratively while retaining the precise pixel-level spectral
695 information. When the MLP is used alone for iteration, the process will lead to model overfitting
696 towards training samples and failure to capture the spatial context relevant to LU (e.g.,
697 commercial areas involve large buildings and retail together with parking lots). Using the CNN
698 only through iteration will result in blurred object boundaries within the classification results
699 caused by the densely overlapping patches and spatial convolution, thereby missing fine-scale
700 detail and degrading the classification accuracy (Zhang *et al.*, 2018c). By combining the MLP
701 and CNN in a hierarchy, the blurred boundaries in the LU obtained by the patch-based CNN can
702 be pulled back to the pixel-level detail in the LC by employing the MLP classifier. Similarly, the
703 spatial context of the neighbourhood information in the LU is utilised by the MLP to support the
704 production of a less noisy and more accurate LC classification. Such joint classification
705 formulates a cyclic process of information as: “neighbourhood – pixel – neighbourhood – pixel”,
706 where the precise LU and LC are characterised through the appropriate hierarchical
707 representation and in a joint fashion.

708 Together with the scale sequence and integrated hierarchical learning, the proposed SS-JDL is,
709 therefore, parsimonious with high computational efficiency, and effective in that it delivers
710 superior classification accuracy relative to benchmarks, some of which can be considered to be

711 state-of-the-art. Both efficiency due to simplicity and effectiveness in accuracy were supported
712 by the experimental results, in which the SS-JDL constantly achieved the highest classification
713 accuracies for LU and LC with the least computational time in both study areas.

714 From an artificial intelligence perspective, the SS-JDL mimics the human visual system,
715 combining the information across multiple scales to increase semantic meanings through joint
716 reinforcement processes. Within the SS-JDL, the information learnt from lower scales passes
717 forward to the higher scales, and high-level semantic information is learned gradually through
718 continuously increasing window sizes of the CNN. Likewise, the human visual system can
719 capture high level semantic representations (e.g., LU feature representations) without conscious
720 effort, and such that the spatial outlines and the fine grained detail are integrated for vision and
721 image understanding. Human brains are not required to exhaustively search for the so-called
722 “optimal” scales, but rather are able to identify and label objects with both low and higher-order
723 semantic meaning, drawing from labels that exist in a changing hierarchical ontological
724 relationship, with great ability for generalisation and practical utility. The joint reinforcement in
725 SS-JDL across scales, therefore, has great potential to catalyse a step change in the future of
726 machine learning and AI, as well as applications in remote sensing and machine vision.

727 **5 Conclusion**

728 Scale effects are a fundamental concern in remotely sensed image classification and are
729 manifested in the landscapes to be classified. For land use (LU) classification and land cover
730 (LC), it has been demonstrated that *greatly* increased classification accuracy for both can be
731 achieved by predicting LU using an object-based CNN, predicting LC via an MLP, and
732 modelling explicitly the relationship between the predicted LU and LC variables as a joint
733 distribution (Zhang *et al.*, 2019), thus, representing the obvious hierarchical relationship between
734 LU and LC in both the scale and the ontological sense. However, its implementation requires the
735 selection of an optimal patch size for the OCNN, which requires extensive searching and is, thus,

736 computationally expensive. In this paper, an innovative scale sequence joint deep learning (SS-
737 JDL) framework, that involves the same MLP and OCNN classification models, was proposed
738 for joint LU and LC classification. Based on the minimum and the maximum sizes of image
739 objects, the SS-JDL method autonomously incorporates multiple scales within its iterative
740 process, such that it removes the requirement for tedious optimal scale selection. The
741 experimental results demonstrate excellent classification accuracy and computational efficiency
742 in comparison with the benchmark methods, including the recently proposed joint deep learning
743 (JDL) method. The proposed method is simple to implement, and has great generalisation
744 capability and practical utility with the default parameter settings. The SS-JDL, therefore, has
745 the potential to transform image classification in the field of remote sensing, and machine
746 learning generally, by creating a fast and effective implementation of the unifying joint deep
747 learning (JDL) framework for classifying higher order feature representations, including LU in
748 the context of remote sensing.

749 **Acknowledgements**

750 This research was funded by the Centre of Excellence in Environmental Data Science (CEEDS),
751 jointly sponsored by Lancaster University and UKRI Centre for Ecology & Hydrology. The
752 research was supported by the National Key R&D Program of China (Grant No.
753 2016YFB0502300) and partially funded by the National Natural Science Foundation of China
754 (41871236). The authors are grateful to the Ordnance Survey for providing the aerial imagery
755 and ground data.

756

757 **References**

758 Arel, I., Rose, D.C., Karnowski, T.P., 2010. Deep machine learning - A new frontier in
759 artificial intelligence research. *IEEE Comput. Intell. Mag.* 5, 13–18.

760 <https://doi.org/10.1109/MCI.2010.938364>

761 Atkinson, P.M., Tatnall, A.R.L., 1997. Introduction Neural networks in remote sensing. *Int. J.*
762 *Remote Sens.* 18, 699–709. <https://doi.org/10.1080/014311697218700>

763 Chen, S., Tian, Y., 2015. Pyramid of spatial relations for scene-level land use classification.
764 *IEEE Trans. Geosci. Remote Sens.* 53, 1947–1957.
765 <https://doi.org/10.1109/TGRS.2014.2351395>

766 Cheng, G., Wang, Y., Xu, S., Wang, H., Xiang, S., Pan, C., 2017. Automatic road detection
767 and centerline extraction via cascaded end-to-end Convolutional Neural Network. *IEEE*
768 *Trans. Geosci. Remote Sens.* 55, 3322–3337.
769 <https://doi.org/10.1109/TGRS.2017.2669341>

770 Del Frate, F., Pacifici, F., Schiavon, G., Solimini, C., 2007. Use of neural networks for
771 automatic classification from high-resolution images. *IEEE Trans. Geosci. Remote Sens.*
772 45, 800–809. <https://doi.org/10.1109/TGRS.2007.892009>

773 Dong, Y., Zhang, Liangpei, Zhang, Lefei, Du, B., 2015. Maximum margin metric learning
774 based target detection for hyperspectral images. *ISPRS J. Photogramm. Remote Sens.*
775 108, 138–150. <https://doi.org/10.1016/j.isprsjprs.2015.07.003>

776 He, N., Paoletti, M.E., Haut, J.M., Fang, L., Li, S., Plaza, A., Plaza, J., 2019. Feature extraction
777 with multiscale covariance maps for hyperspectral image classification. *IEEE Trans.*
778 *Geosci. Remote Sens.* 57, 755–769. <https://doi.org/10.1109/TGRS.2018.2860464>

779 Herold, M., Liu, X., Clarke, K.C., 2003. Spatial Metrics and Image Texture for Mapping Urban
780 Land Use. *Photogramm. Eng. Remote Sens.* 69, 991–1001.
781 <https://doi.org/10.14358/PERS.69.9.991>

782 Hu, F., Xia, G.-S., Hu, J., Zhang, L., 2015. Transferring deep Convolutional Neural Networks

783 for the scene classification of high-resolution remote sensing imagery. *Remote Sens.* 7,
784 14680–14707. <https://doi.org/10.3390/rs71114680>

785 Hu, S., Wang, L., 2013. Automated urban land-use classification with remote sensing. *Int. J.*
786 *Remote Sens.* 34, 790–803. <https://doi.org/10.1080/01431161.2012.714510>

787 Kim, M., Warner, T.A., Madden, M., Atkinson, D.S., 2011. Multi-scale GEOBIA with very
788 high spatial resolution digital aerial imagery: scale, texture and image objects. *Int. J.*
789 *Remote Sens.* 32, 2825–2850. <https://doi.org/10.1080/01431161003745608>

790 Krizhevsky, A., Sutskever, I., Hinton, G.E., 2012. ImageNet classification with deep
791 Convolutional Neural Networks, in: *NIPS2012: Neural Information Processing Systems.*
792 *Lake Tahoe, Nevada*, pp. 1–9.

793 Långkvist, M., Kiselev, A., Alirezaie, M., Loutfi, A., 2016. Classification and segmentation of
794 satellite orthoimagery using Convolutional Neural Networks. *Remote Sens.* 8, 1–21.
795 <https://doi.org/10.3390/rs8040329>

796 Lappe, M., Kruger, N., Leonardis, A., Janssen, P., Piater, J., Wiskott, L., Rodriguez-Sanchez,
797 A.J., Kalkan, S., 2013. Deep Hierarchies in the Primate Visual Cortex: What Can We
798 Learn for Computer Vision? *IEEE Trans. Pattern Anal. Mach. Intell.* 35, 1847–1871.
799 <https://doi.org/10.1109/tpami.2012.272>

800 LeCun, Y., Bengio, Y., Hinton, G., 2015. Deep learning. *Nature* 521, 436–444.
801 <https://doi.org/10.1038/nature14539>

802 Li, Q., Mou, L., Liu, Q., Wang, Y., Zhu, X.X., 2018. HSF-Net: Multiscale deep feature
803 embedding for ship detection in optical remote sensing imagery. *IEEE Trans. Geosci.*
804 *Remote Sens.* 56, 7147–7161. <https://doi.org/10.1109/TGRS.2018.2848901>

805 Li, Y., Wang, N., Shi, J., Hou, X., Liu, J., 2018. Adaptive Batch Normalization for practical

806 domain adaptation. *Pattern Recognit.* 80, 109–117.
807 <https://doi.org/10.1016/j.patcog.2018.03.005>

808 Liu, X., He, J., Yao, Y., Zhang, J., Liang, H., Wang, H., Hong, Y., 2017. Classifying urban
809 land use by integrating remote sensing and social media data. *Int. J. Geogr. Inf. Sci.* 31,
810 1675–1696. <https://doi.org/10.1080/13658816.2017.1324976>

811 Liu, Y., Guan, Q., Zhao, X., Cao, Y., 2018. Scene Classification Based on Multiscale
812 Convolutional Neural Network. *IEEE Trans. Geosci. Remote Sens.* 56, 7109–7121.

813 Lv, X., Ming, D., Lu, T., Zhou, K., Wang, M., Bao, H., 2018. A new method for region-based
814 majority voting CNNs for very high resolution image classification. *Remote Sens.* 10, 1–
815 24. <https://doi.org/10.3390/rs10121946>

816 Ming, D., Li, J., Wang, J., Zhang, M., 2015. Scale parameter selection by spatial statistics for
817 GeOBIA: Using mean-shift based multi-scale segmentation as an example. *ISPRS J.*
818 *Photogramm. Remote Sens.* 106, 28–41. <https://doi.org/10.1016/j.isprsjprs.2015.04.010>

819 Nogueira, K., Penatti, O.A.B., dos Santos, J.A., 2017. Towards better exploiting convolutional
820 neural networks for remote sensing scene classification. *Pattern Recognit.* 61, 539–556.
821 <https://doi.org/10.1016/j.patcog.2016.07.001>

822 Pan, X., Zhao, J., 2018. High-Resolution Remote Sensing Image Classification Method Based
823 on Convolutional Neural Network and Restricted Conditional Random Field. *Remote*
824 *Sens.* 10, 1–20. <https://doi.org/10.3390/rs10060920>

825 Romero, A., Gatta, C., Camps-valls, G., Member, S., 2016. Unsupervised deep feature
826 extraction for remote sensing image classification. *IEEE Trans. Geosci. Remote Sens.* 54,
827 1349–1362. <https://doi.org/10.1109/TGRS.2015.2478379>.

828 Stürck, J., Schulp, C.J.E., Verburg, P.H., 2015. Spatio-temporal dynamics of regulating

829 ecosystem services in Europe- The role of past and future land use change. *Appl. Geogr.*
830 63, 121–135. <https://doi.org/10.1016/j.apgeog.2015.06.009>

831 Wang, H., Wang, Y., Zhang, Q., Xiang, S., Pan, C., 2017. Gated convolutional neural network
832 for semantic segmentation in high-resolution images. *Remote Sens.* 9, 1–15.
833 <https://doi.org/10.3390/rs9050446>

834 Wu, S.S., Qiu, X., Usery, E.L., Wang, L., 2009. Using geometrical, textural, and contextual
835 information of land parcels for classification of detailed urban land use. *Ann. Assoc. Am.*
836 *Geogr.* 99, 76–98. <https://doi.org/10.1080/00045600802459028>

837 Yang, Z., Mu, X. dong, Zhao, F. an, 2018. Scene classification of remote sensing image based
838 on deep network and multi-scale features fusion. *Optik (Stuttg.)*. 171, 287–293.
839 <https://doi.org/10.1016/j.ijleo.2018.06.024>

840 Zhang, C., Pan, X., Li, H., Gardiner, A., Sargent, I., Hare, J., Atkinson, P.M., 2018a. A hybrid
841 MLP-CNN classifier for very fine resolution remotely sensed image classification. *ISPRS*
842 *J. Photogramm. Remote Sens.* 140, 133–144.
843 <https://doi.org/10.1016/j.isprsjprs.2017.07.014>

844 Zhang, C., Sargent, I., Pan, X., Gardiner, A., Hare, J., Atkinson, P.M., 2018b. VPRS-based
845 regional decision fusion of CNN and MRF classifications for very fine resolution
846 remotely sensed images. *IEEE Trans. Geosci. Remote Sens.* 56, 4507–4521.
847 <https://doi.org/10.1109/TGRS.2018.2822783>

848 Zhang, C., Sargent, I., Pan, X., Li, H., Gardiner, A., Hare, J., Atkinson, P.M., 2019. Joint Deep
849 Learning for land cover and land use classification. *Remote Sens. Environ.* 221, 173–187.
850 <https://doi.org/10.1016/j.rse.2018.11.014>

851 Zhang, C., Sargent, I., Pan, X., Li, H., Gardiner, A., Hare, J., Atkinson, P.M., 2018c. An
852 object-based convolutional neural network (OCNN) for urban land use classification.

853 Remote Sens. Environ. 216, 57–70. <https://doi.org/10.1016/j.rse.2018.06.034>

854 Zhao, B., Zhong, Y., Zhang, L., 2016. A spectral-structural bag-of-features scene classifier for
855 very high spatial resolution remote sensing imagery. ISPRS J. Photogramm. Remote Sens.
856 116, 73–85. <https://doi.org/10.1016/j.isprsjprs.2016.03.004>

857 **List of Figure Captions**

858 Figure 1. The general workflow of scale sequence joint deep learning (SS-JDL) for land cover
859 and land use classification.

860 Figure 2. Three study areas: Bournemouth (S1), Southampton (S2) and Manchester (S3) in
861 England, with typical land use categories highlighted for each study site.

862 Figure 3. Model structures and architectures of the deep CNN network with nine hidden layers.

863 Figure 4. The influence of iteration upon overall accuracy for the LU and LC classifications
864 using the proposed SS-JDL and the JDL method.

865 Figure 5. The effects of window size (scale) on overall accuracy of the LU and LC classifications
866 using the SS-JDL (dashed lines) and the JDL method (solid lines).

867 Figure 6. Three subset (i.e., a, b, c) of LC classification in S1 using Scale Sequence Joint Deep
868 Learning (SS-JDL) from iteration 1 (28×28) to 5 (140×140). The correct and incorrect
869 classifications are highlighted by circles in yellow and red, respectively.

870 Figure 7. Three subset (i.e., a, b, c) of LC classification in S2 using Scale Sequence Joint Deep
871 Learning (SS-JDL) from iteration 1 (28×28) to 5 (140×140). The correct and incorrect
872 classifications are highlighted by circles in yellow and red, respectively.

873 Figure 8. The land cover classification in S3 using Scale Sequence Joint Deep Learning (SS-
874 JDL) from iteration 1 (28×28) to 5 (140×140).

875 Figure 9. Three subset (i.e., a, b, c) of LU classification in S1 using Scale Sequence Joint Deep
876 Learning (SS-JDL) from iteration 1 (28×28) to 5 (140×140). The correct and incorrect
877 classifications are highlighted by circles in yellow and red, respectively.

878 Figure 10. Three subset (i.e., a, b, c) of LU classification in S2 using Scale Sequence Joint Deep
879 Learning (SS-JDL) from iteration 1 (28×28) to 5 (140×140). The correct and incorrect
880 classifications are highlighted by circles in yellow and red, respectively.

881 Figure 11. The land use classification in S3 using Scale Sequence Joint Deep Learning (SS-JDL)
882 from iteration 1 (28×28) to 5 (140×140).

883 Figure 12. Image subset benchmark comparison among various methods for S1, S2 and S3. The
884 LC classifications include (a) MLP, (b) GLCM-MLP, (c) MRF, (d) MCNN-LC, (e) JDL-LC,
885 and the (f) SS-JDL-LC. The LU classifications include (g) MRF, (h) OBIA, (i) CNN, (j) MCNN
886 -LU, (k) JDL-LU, and the (l) SS-JDL-LU. Refer to Figures 6 to 11 for details of the
887 corresponding classification legends.

888